In-Duct Matching Strategies

FINAL REPORT AND CONCLUSIONS

TURBONOISECFD WORKPACKAGE 2

PART OF DELIVERABLE D2.4

by

N.C. Ovenden & S.W. Rienstra
Department of Mathematics and Computer Science
Eindhoven University of Technology
P.O.Box 513, 5600 MB Eindhoven
The Netherlands

August 14, 2002

Contents

In-duct matching strategies

N.C. Ovenden and S.W. Rienstra
Eindhoven University of Technology
P.O.Box 513, 5600 MB Eindhoven
The Netherlands
August 14, 2002

Summary

The matching problem within an engine duct is considered across the interface between a region with CFD-type full Navier-Stokes modelling (the source region) and a region (duct) assumed only to contain a mean flow plus small acoustic perturbations. A discontinuity in the flow field variables at this interface cannot be avoided. A discontinuous mean flow will produce spurious reflections if conditions of smoothness on the acoustic field are given the highest priority. A careful distinction between ingoing and outgoing waves at the interface is necessary to recognise, capture and suppress the physically undesirable false reflections. Therefore methods are proposed, based on a modal representation of the acoustic field, to determine the transition across the interface of the field as accurately as possible by means of a least squares modification of a Galerkin-type mode matching. These least squares methods are then tested using real CFD data and compared to traditional matching strategies. The results enable us to put forward a possible optimal matching strategy, which requires pressure data at three neighbouring axial locations.

The triple-plane (multi-plane) pressure matching strategy is originally defined within a locally parallel duct. However, we demonstrate that it is possible to extend the strategy using the theory of multiple-scales to enable matching to be performed in converging and diverging ducts. The method can be applied to regions of the ducts with both hard and impedance walls, although more work is required to assess fully the effect of the non-orthogonality of impedance-wall modes.

1 Introduction

1.1 The CFD and acoustic zones and their interfaces

In the CFD regions (fig.1, or zones 4,6,7,15 in fig.2) the unsteady parts of all flow variables like pressure, velocity, density and possibly the thermodynamic variables are of the same order of magnitude as the steady (time-averaged) parts. In the acoustic regions (zones 1,3,5,8,9, 10,16,18 in fig.2) the unsteady components are small compared to the steady (mean) flow. Therefore, the way the CFD flow is

determined is very different, and usually numerically more advanced and calculation-intensive, than the acoustic field.

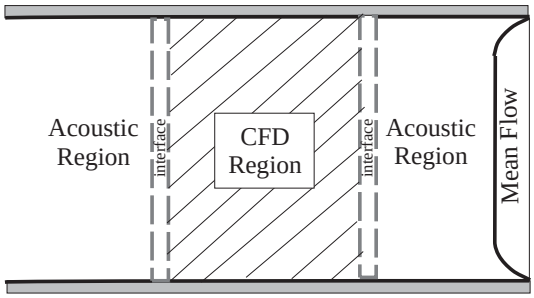

Figure 1: Sketch of CFD region, acoustic region and interfaces.

Apart from that, the underlying models may vary considerably. The flow may be (Reynolds-averaged turbulent) viscous, isentropic, irrotational, cylindrical symmetric, of single frequency, etc.

Therefore, to translate the CFD results (pressure, velocity) into a form suitable for serving as a source in the acoustic problem is not straightforward.

1.2 Continuity of acoustic field

At the interfaces (see fig.1) we jump from model $\mathcal{A}$ (the full Navier-Stokes, say) into model $\mathcal{B}$ (inviscid flow with acoustic perturbations, say). The mean flow variables that are consistent within model $\mathcal{A}$ are almost certainly not consistent within model $\mathcal{B}$. In other words, they do not satisfy the equations. Therefore, some of the field variables (both of mean flow and perturbation) will have to be discontinuous at the interface. Any attempt to make more than one of the acoustic variables continuous has to be paid by a just as unphysical and artificial reflected field.

All this is an artefact of the fact that we change from one model to another and these reflections should be considered just as much of an error as the discontinuities. However, the CFD results are produced without taking into account any back-reaction, such that the field at the interface is as much as possible outgoing. Therefore, we should consider the possibility of minimizing both the reflections and the discontinuities.

As practically all reflections are unphysical (with some exceptions), it seems best to *define* somehow the field at the interface as unidirectionally outgoing. To achieve this, the equations should be solved at least locally near the interface such that incoming and outgoing waves can be separated. This may be approached in various ways. First is an acoustic analogy approach (FW-H, or Kirchhoff type), where the interface is suitably applied with flow sources [1, 2]; this method was not used for the in-duct matching. The second route is the idea of a local parabolic approximation or wave splitting [3, 4] and is most conveniently applied to a modal representation of the sound field, if available.

1.3 Reflection free boundary conditions

Ideally, the CFD flow is computed with reflection-free boundary conditions. To formulate such boundary conditions is a significant problem in its own right and an important part of the CFD calculations. Strictly speaking, it is separate from the matching problem and in practice it can only be achieved by manipulations, similar to the ones we are going to deal with here.

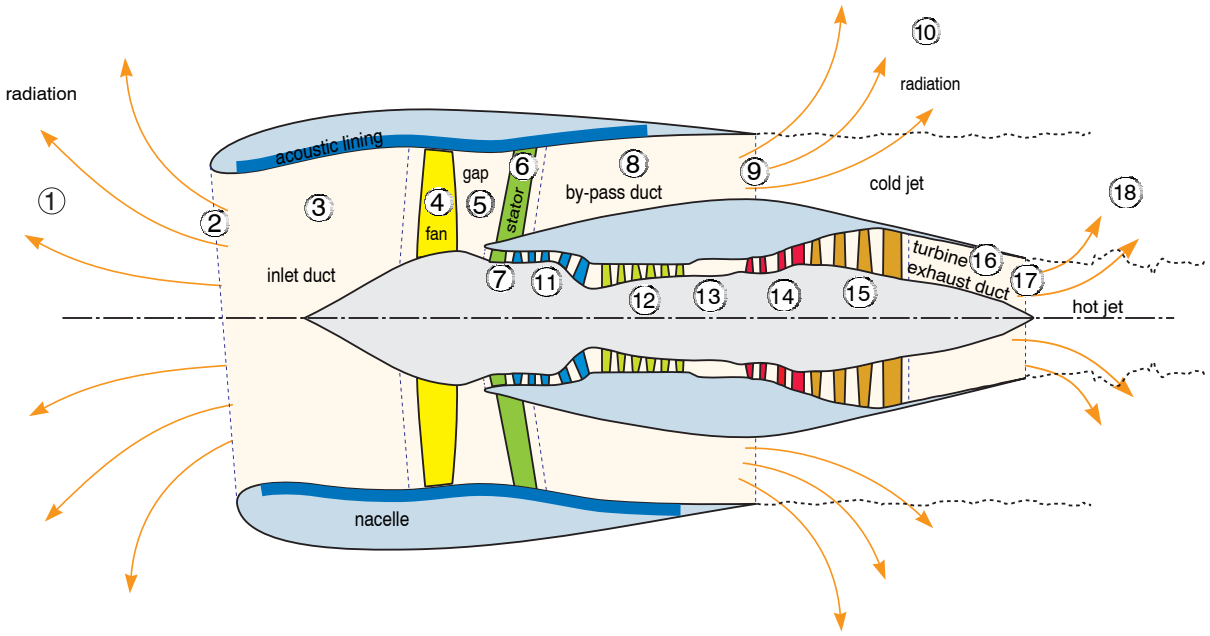

Figure 2: The zones in a typical high-bypass ratio turbofan engine.

To eliminate false reflections from the interface in the CFD results, a CFD model $\mathcal{A}$ may at or near the interface be approximated by a simpler model $\widetilde{\mathcal{A}}$ (usually one which is valid for inviscid linear perturbations and without the turbulence model included). This model can be solved analytically and the right- and left-running waves can then be separated (wave splitting).

In order to continue beyond the interface, into the acoustic region with an acoustic model $\mathcal{B}$, we will do something similar. We will try to continue the CFD field smoothly into the acoustic field of model $\mathcal{B}$ and to recognize the spurious reflected modes resulting from the jump between model $\mathcal{A}$ and $\mathcal{B}$. So even if the CFD results are ideal and reflection free in some sense, there will inevitably be false reflections from the non-ideal jump from model $\mathcal{A}$ to $\mathcal{B}$.

Rather than assuming the CFD field to be reflection free and not even considering the possibility of a reflected field, it seems therefore a better strategy to include in the matching the detection of reflected modes. Of course, after detection these modes play no role in the acoustic problem and may be discarded.

1.4 The character of the jump

The ideal situation would be to have the interface (between the CFD and the acoustic region) positioned far enough into the acoustic region, so that the acoustic equations are equivalent to the Navier-Stokes equations. We can then continue with either the given pressure or axial velocity distribution, p or v.

The real situation, however, is that the interface is positioned as close to the source region as possible and we have to deal with a discontinuity in almost every mean flow variable. The acoustic field will then have to be discontinuous in some quantities. A question may be: which quantities should one make as continuous as possible ?

As the CFD is nonlinear and the acoustic model is linear, the mean flow and acoustic mean flow will differ. In addition, the acoustic model is usually based on a simpler flow (irrotational, isentropic, inviscid, no swirl, etc.). Hence the "model-jump" is not always the same and the risk of an artificial source hidden in the interface will depend both on the mean flow and on the acoustic field model considered.

1.5 The mean flow

As mentioned above, one difficulty with the matching is the need to translate the CFD mean flow into a simpler acoustic mean flow which is *acceptable* to the acoustic model B. We could define the CFD mean flow as the time-averaged CFD flow, while the unsteady part is defined as the acoustic and hydrodynamic perturbations. Note that (in the case of steady boundaries) this mean flow does not satisfy the steady version of the CFD problem (steady Euler, Navier Stokes, etc.) and that this perturbation does not exactly satisfy the linearized equations if the flow remains nonlinear.

As the various models are in general not equivalent, the mean flow obtained is still unable to satisfy the basic assumptions of the acoustic model. Therefore, the mean flow has to be stripped further to remove: swirl, entropy variations, vorticity and any strong radial component.

1.6 Modal decomposition

The wave splitting via modal decomposition is probably the best, or at least systematic, way to bring the CFD perturbations into an acoustic form. It hinges on the availability of generation of modes in cylindrical ducts with mean flow.

For plug flow (as assumed in our real data tests) the situation is fairly well established. Modes are formed by linear combinations of Bessel functions, while the eigenvalues are zeros of the derivatives. The modes are orthogonal, so there are no uniqueness problems. Hydrodynamic modes are pressureless (see below) which may confuse a description based on acoustic modes alone, but this seems to be a minor problem.

For parallel mean flow we have the Pridmore-Brown equation, for which the eigenvalue problem is more complicated, but it is solvable with the right numerical software; it may become problematic for higher frequencies. Modes are not orthogonal, so the amplitudes associated to a finite number are not unique. Hydrodynamic modes are also present.

For uniform mean flow with swirl, the mode problem [5, 6] becomes more and more complicated, especially if the swirl is arbitrary. Solid body rotation or free vortex swirl are relatively well studied. A natural next step appears to be the integration of the present method with the results reported under [7, 8], possibly in connection with its extension to slowly varying ducts in [9].

Little is known for more general parallel mean flow with swirl.

1.7 Hard wall

It is definitely easier to assume that the interface is positioned in a hard-walled section. This may not always be realistic, for example, the fan rotor section may be lined. However, most CFD routines seem not to be equipped with lined boundary conditions. Therefore, we will start by assuming hard walls.

1.8 Summary of acoustic models and modal solutions

For future reference we have summarized in the appendix a large number of possible acoustic models, together with further simplifications and solution approaches. As the matching requires information on the direction of the sound field, emphasis will be given to modal decomposition, which yields this information instantly.

2 Interface conditions

2.1 The interface

In our study, we have assumed the interface to be either a single axial surface plane x_0 or an axially-thin region containing several axial surface planes at x_0, x_1, $x_2 \ldots x_n$. The interface is contained within a locally parallel cylindrical duct with inner and outer walls at $r = R_1$ and $r = R_2$ respectively. A choice of n large may seem the best option at first in order to make use of as much information as possible. However, the fact that each model (CFD and acoustic) obeys different physics suggests that taking too many axial planes, particularly ones lying close to the source, would introduce much larger errors that would prove difficult to minimise. In light of this reasoning, only a small axial range should be examined but with enough data to perform a least squares minimisation. For the real data tests presented $n = 3$ was chosen.

To allow more general configurations in the matching process (for example, with swept vanes or blades), the axial surface planes connecting the source region to the rest of the duct can be represented as an axial position $\tilde{x}_i$ added to a radial shape function

$$x_i(r) = \tilde{x}_i + \lambda_i(r). \tag{1}$$

At each axial surface plane x_i the field variables including velocity $\boldsymbol{v}(x, r, \theta, t)$, pressure $p(x, r, \theta, t)$, density $\rho(x, r, \theta, t)$, entropy $s(x, r, \theta, t)$ etc. are given. If we take the most important ones (namely pressure and axial velocity but this is a matter of taste), they can be Fourier-decomposed at the axial plane $x = x_i$ in time and circumferential direction to give the pressure component $\mathcal{P}_{\omega mi}(r)$ and axial velocity component $\mathcal{U}_{\omega mi}(r)$ for a given angular frequency ω (Helmholtz number) and circumferential mode m; see section 8 and the appendix for more details. The axisymmetric mean flow can be taken as the $(\omega, m) = (0, 0)$ component. As they are the product of another model (*e.g.* , CFD based on RANS), it is almost inevitable and that they will not be consistent with the simpler acoustic model.

We now have the following options.

Traditional mode matching:

(i) At a single axial surface plane, assume that one of the field variables (ideally pressure) should be continuous, *i.e.* prescribed by the source region at the interface. The other field variables of the resulting field will be discontinuous at the interface. In this case it is not possible to include all incoming and outgoing waves because the resulting field would radiate symmetrically away from the interface and comprise of about as many incoming waves as outgoing waves. In other words, the amplitudes would be about half of what they should be.

Therefore, with this option it is not only natural but also necessary to assume beforehand that the incoming waves are absent.

(ii) To take into account the fact that the CFD non-reflecting boundary condition is not perfect and that the resultant field is not yet free of spurious reflections, we can try to include both reflected (incoming) and transmitted (outgoing) waves. On physical grounds (see option i), we then need to specify continuity at a single axial surface plane of a second variable (axial velocity). This is the usual direct approach and requires careful book keeping of matrices. Furthermore, one must be careful to ensure that the velocity perturbation is not contaminated by vorticity. Otherwise, the calculated sound field will not be physically correct and gross underestimates or overestimates of the sound power level may be made.

(iii) In order to include reflected waves whilst avoiding errors due to the likelihood that the velocity contains a strong vortical part, we can make the axial pressure gradient continuous instead of the axial velocity. The pressure gradient can be derived at a particular axial surface plane from pressure data provided on neighbouring axial surface planes (via a simple central difference for example).

Least Squares Matching:

(iv) If we wish to ignore reflections, but utilise more flow-field information than only pressure to spread the discontinuity over several chosen variables at a single axial surface plane, then a least-squares method can be adopted. Once again, an improvement in accuracy can only be achieved if the variables included have a negligible vortical or otherwise non-acoustical part.

(v) Because the least-squares method can minimise the discontinuity across as many variables as one wishes, it seems sensible to try to include the information at several axial surface planes. So long as more than one variable at a single axial surface plane is employed, reflected waves can also be resolved (or not, as required). One advantage of this approach is that the reflected (incoming) waves can be determined just from pressure information at two or more surface planes without any reliance on velocity information. The procedure is also simpler than a direct matching with additionally no need to determine numerically the axial pressure gradient. However, it is difficult to say without a closer examination whether the directional information can be extracted from the small pressure or velocity changes that occur between neighbouring interfaces.

Note that in all cases where the reflected (incoming) waves are resolved, the reflections are a *mix* of the effects of the imperfect CFD radiation condition and the inherent modelling discontinuity. As we argued before, there is absolutely no reason to include reflections due to the modelling jump. Therefore, this option is only useful if this jump is small and the acoustic model is *practically equivalent* to the linearized version of the CFD model.

It is not our intention to consider the possibility that the spurious reflections are (iteratively) coupled back to the CFD calculations, such that these reflections are made to vanish. This is practically only possible if both CFD and acoustic calculations are run in parallel on the same computer.

From the above statements, one might argue that there is no real need to include reflected waves and that it is sufficient to apply the method to the outgoing waves only. Although this is true in principle, there are still a few good reasons to at least investigate the possibility: (1) as we will see, the amount of work and programming is practically the same as for the unidirectional options; (2) the filtering of false reflections would have been the final postprocessing of the CFD calculations anyway and if the acoustic model is not simpler than the reduced CFD model "$\widetilde{\mathcal{A}}$" (see section 1.3), it is just as efficient to do it here; (3) the amount of reflected sound is a possible measure of the interface mismatch, which may be a useful diagnostic quantity for later analysis.

The principal objective of this report is to compare the traditional matching methods (i), (ii) and (iii) with the more novel least-squares and multi-plane methods (iv) and (v) in order to find an optimal strategy. Each of these methods is described in more mathematical detail in section 3 and the results of experiments on real CFD data are presented in section 4. The results of the real data tests reveal not only a possible optimal strategy, but that multi-plane matching strategies have many other benefits in terms of understanding and error checking that single axial surface plane methods do not.

3 Mode matching

If we have found the modal basis functions of all field variables, both incoming (reflected) and outgoing (transmitted), we can write our field as a formal series expansion over these basis functions. Suppose that the *outgoing* basis functions of the (ω, m) pressure contribution p_m are the set $\psi_{m\mu}(r)$ with $\mu > 0$ and the *incoming* are the set $\psi_{m\mu}(r)$ with $\mu < 0$.

For the investigation, we will consider five approaches, which were defined in section 2.1. The first three (options i,ii and iii) can be regarded as traditional methods of mode matching where continuity of either one or two flow variables is specified, depending on whether only outgoing modes or both incoming and outgoing modes are assumed to be present. The final two strategies (options iv and v) are more advanced and based on a least squares approach, where incoming reflected modes may be included or not. In addition, the final option (option v) extends this approach from a single axial surface plane to multiple axial surface planes.

Under the assumption of completeness, as discussed in the appendix, we can write the resulting outgoing (ω, m) pressure component (or any other variable) in the following way:

$$p_{\omega m}(x, r) = \sum_{\mu=1}^{M} \tilde{A}_{m\mu} \psi_{m\mu}(r)\, \mathrm{e}^{-\mathrm{i}\kappa_{m\mu} x}, \tag{2}$$

where $\kappa_{m\mu}$ is the axial eigenvalue (wavenumber) of mode μ, M is the number of modes considered and $\tilde{A}_{m\mu}$ are the *modal* amplitudes.

If the pressure is to be continuous at the interface (in this case at a single axial surface plane at x_0) and we do not include possible reflections, we have thus

$$\sum_{\mu=1}^{M} \tilde{A}_{m\mu} \psi_{m\mu}(r)\, \mathrm{e}^{-\mathrm{i}\kappa_{m\mu}(\tilde{x}_0 + \lambda_0(r))} = \mathcal{P}_{\omega m0}(r), \tag{3}$$

and the modal amplitudes are found by the following Galerkin-type procedure.

We form an (L_2) inner product, between the left- and right-hand sides and a suitable set of test functions, by integration along the cross section of the interface, *i.e.* between R_1 to R_2. Usually, the complex conjugate of the basis functions themselves are convenient for this purpose, especially when they are orthogonal or nearly orthogonal under the defined inner product. We choose here $\psi^*_{m\nu}(r)\, \mathrm{e}^{\mathrm{i}\kappa^*_{m\nu}\lambda_0(r)}$, $\nu = 1, \ldots, M$, to obtain

$$\sum_{\mu=1}^{M} \tilde{A}_{m\mu}\, \mathrm{e}^{-\mathrm{i}\kappa_{m\mu}\tilde{x}_0} \int_{R_1}^{R_2} \psi_{m\mu}(r)\psi^*_{m\nu}(r)\, \mathrm{e}^{-\mathrm{i}(\kappa_{m\mu} - \kappa^*_{m\nu})\lambda_0(r)}\, r\, \mathrm{d}r = \int_{R_1}^{R_2} \mathcal{P}_{\omega m0}(r)\psi^*_{m\nu}(r)\, \mathrm{e}^{\mathrm{i}\kappa^*_{m\nu}\lambda_0(r)}\, r\, \mathrm{d}r, \tag{4}$$

or in matrix form

$$\mathcal{M}\boldsymbol{a} = \boldsymbol{p}, \tag{5}$$

where

$$\{\mathcal{M}\}_{\nu\mu} = \int_{R_1}^{R_2} \psi_{m\mu}(r)\psi^*_{m\nu}(r)\,\mathrm{e}^{-\mathrm{i}(\kappa_{m\mu}-\kappa^*_{m\nu})\lambda_0(r)}\,r\,\mathrm{d}r \tag{6a}$$

$$\{\boldsymbol{a}\}_{\mu} = \tilde{A}_{m\mu}\,\mathrm{e}^{-\mathrm{i}\kappa_{m\mu}\tilde{x}_0} = A_{m\mu} \tag{6b}$$

$$\{\boldsymbol{p}\}_{\nu} = \int_{R_1}^{R_2} \mathcal{P}_{\omega m0}(r)\psi^*_{m\nu}(r)\,\mathrm{e}^{\mathrm{i}\kappa^*_{m\nu}\lambda_0(r)}\,r\,\mathrm{d}r. \tag{6c}$$

With this choice of test functions the matrix $\mathcal{M}$ is then hermitian. This means that the transposed complex conjugate, *i.e.* $\mathcal{M}^* = \overline{\mathcal{M}}^{\top}$, is equal to $\mathcal{M}$ itself: $\mathcal{M}^* = \mathcal{M}$, leading to the important consequences that $\mathcal{M}$'s eigenvalues are real and $\mathcal{M}$'s eigenvectors are orthogonal. An even more important consequence here is the relatively simple form that the solution of the least-squares problem, defined below, attains. Therefore, we will assume in the analysis below that the test functions are chosen so that $\mathcal{M}$ is hermitian.

Now we can construct solutions according to the approaches proposed in section 2.1. For the sake of clarity, we shall assume the axial surface planes to be constant axial planes $\lambda_i(r) = 0$; the analysis is easily extended to non-constant axial planes by adding the extra exponential terms given in the expressions above, but **only** if the duct remains straight and non-varying locally. We shall also rescale the modal amplitudes by shifting the origin to $x = x_0$ via the transform $A_{m\mu} = \tilde{A}_{m\mu}\,\mathrm{e}^{-\mathrm{i}\kappa_{m\mu}x_0}$.

3.1 Single variable (option i)

Here is the direct way, where only one variable (almost certainly pressure) is taken to be continuous at a single axial plane and the other field variables are ignored. As discussed in section 2.1(i), we do not account for false reflections, so we have

$$p_{\omega m}(x, r) = \sum_{\mu=1}^{M} A_{m\mu}\psi_{m\mu}(r)\,\mathrm{e}^{-\mathrm{i}\kappa_{m\mu}(x-x_0)}, \tag{7}$$

$$\sum_{\mu=1}^{M} A_{m\mu}\int_{R_1}^{R_2} \psi_{m\mu}(r)\psi^*_{m\nu}(r)r\,\mathrm{d}r = \int_{R_1}^{R_2} \mathcal{P}_{\omega m0}(r)\psi^*_{m\nu}(r)r\,\mathrm{d}r. \tag{8}$$

Using the same nomenclature as given by equations (6) for a constant axial plane, the amplitude vector is then (formally) given by

$$\boldsymbol{a} = \mathcal{M}^{-1}\boldsymbol{p} \tag{9}$$

and may be obtained by standard numerical techniques.

3.2 Direct matching including reflections (option ii and iii)

In this case, two variables are taken to be continuous at a single axial plane and the other field variables are ignored. For this to be possible, reflected modes must be included. Assuming we consider the (ω, m) pressure component $p_{\omega m}(x, r)$, with basis functions $\psi_{m\mu}$, and either the (ω, m) *irrotational* axial velocity

component (option ii) or the (ω, m) axial pressure gradient component (option iii) $u_{\omega m}(x, r)$, with basis functions $\chi_{m\mu}$, then we write

$$p_{\omega m}(x, r) = \sum_{\mu=1}^{M} A_{m\mu}\psi_{m\mu}(r)\,\mathrm{e}^{-\mathrm{i}\kappa_{m\mu}(x-x_0)} + \sum_{\mu=-M}^{-1} A_{m\mu}\psi_{m\mu}(r)\,\mathrm{e}^{-\mathrm{i}\kappa_{m\mu}(x-x_0)}, \tag{10a}$$

$$u_{\omega m}(x, r) = \sum_{\mu=1}^{M} A_{m\mu}\chi_{m\mu}(r)\,\mathrm{e}^{-\mathrm{i}\kappa_{m\mu}(x-x_0)} + \sum_{\mu=-M}^{-1} A_{m\mu}\chi_{m\mu}(r)\,\mathrm{e}^{-\mathrm{i}\kappa_{m\mu}(x-x_0)}, \tag{10b}$$

expressing both as a sum of outgoing and incoming waves; note that, for brevity, we shall now define

$$\sum_{\mu=-M}^{M} = \sum_{\mu=-M}^{-1} + \sum_{\mu=1}^{M},$$

to be the sum over the first M outgoing (transmitted) modes and the first M incoming (reflected) modes. Then, at the single axial plane representing the interface we find

$$\sum_{\mu=-M}^{M} A_{m\mu}\psi_{m\mu}(r) = \mathcal{P}_{\omega m0}(r) = p_{\omega m}(x_0, r), \tag{11a}$$

$$\sum_{\mu=-M}^{M} A_{m\mu}\chi_{m\mu}(r) = \mathcal{U}_{\omega m0}(r) = u_{\omega m}(x_0, r), \tag{11b}$$

where there are $2M$ unknown amplitudes and, therefore, only $2M$ equations are necessary. If the basis functions are L^2-orthogonal (such as in the case of hard walls), these amplitudes can be found uniquely by understanding the relationship that exists between the basis functions $\psi_{m\mu}$ and $\chi_{m\mu}$. Taking the model for uniform mean flow as an example, the functions $\psi_{m\mu}$ and $\chi_{m\mu}$ appear not only very similar to one another, but also to the basis functions of their reflected counterparts $\psi_{m(-\mu)}$ and $\chi_{m(-\mu)}$. In fact, all four can be written as some multiple of a radial function $\zeta_{m|\mu|}$, derived from Bessel functions, in the following way:

$$\psi_{m\mu} = -\mathrm{i}D_0\left(\omega - \kappa_{m\mu}U_0\right)\zeta_{m|\mu|}(r), \tag{12}$$

$$\chi_{m\mu} = -\mathrm{i}\kappa_{m\mu}\zeta_{m|\mu|}(r), \tag{13}$$

for the case where pressure and axial velocity are matched (option ii) or

$$\chi_{m\mu} = -\kappa_{m\mu}D_0\left(\omega - \kappa_{m\mu}U_0\right)\zeta_{m|\mu|}(r), \tag{14}$$

for the case where pressure and axial pressure gradient are matched (option iii). Here D_0 is the non-dimensionalised mean density, U_0 is the non-dimensionalised axial mean flow and ω is the Helmholtz number (scaled using the outer duct radius and reference sound speed). We can then form the (L^2) inner product for both equations in (11) using $\zeta^*_{m\nu}(r)$ for $\nu = 1, \ldots, M$ as a set of M test functions. As a result,

$$\sum_{\mu=-M}^{M} A_{m\mu}\int_{R_1}^{R_2}\psi_{m\mu}(r)\zeta^*_{m\nu}(r)r\,\mathrm{d}r = \int_{R_1}^{R_2}\mathcal{P}_{\omega m0}(r)\zeta^*_{m\nu}r\,\mathrm{d}r, \tag{15}$$

$$\sum_{\mu=-M}^{M} A_{m\mu}\int_{R_1}^{R_2}\chi_{m\mu}(r)\zeta^*_{m\nu}(r)r\,\mathrm{d}r = \int_{R_1}^{R_2}\mathcal{U}_{\omega m0}(r)\zeta^*_{m\nu}r\,\mathrm{d}r, \tag{16}$$

$$\tag{17}$$

to produce $M + M$ equations and the system can be solved by standard numerical techniques.

3.3 Least squares approach at a single axial plane (option iv)

The least squares approach is actually much simpler to formulate than the direct matching, and really involves only a slight extension to the process used in single variable matching (option i) for calculations *both* excluding and including reflections.

Starting with no reflections, assume we consider the (ω, m) components of three variables $p_{\omega m}$, $u_{\omega m}$ and $s_{\omega m}$ (it can be any number), with basis functions $\psi_{m\mu}$, $\chi_{m\mu}$ and $\xi_{m\mu}$ respectively and at $x = x_0$ we are given the CFD source data $p_{\omega m}(x_0, r) = \mathcal{P}_{\omega m0}(r)$, $u_{\omega m}(x_0, r) = \mathcal{U}_{\omega m0}(r)$ and $s_{\omega m}(x_0, r) = \mathcal{S}_{\omega m0}(r)$. Hence,

$$\sum_{\mu=1}^{M} A^{(p)}_{m\mu} \psi_{m\mu}(r) = \mathcal{P}_{\omega m0}(r), \tag{18}$$

$$\sum_{\mu=1}^{M} A^{(u)}_{m\mu} \chi_{m\mu}(r) = \mathcal{U}_{\omega m0}(r), \tag{19}$$

$$\sum_{\mu=1}^{M} A^{(s)}_{m\mu} \xi_{m\mu}(r) = \mathcal{S}_{\omega m0}(r), \tag{20}$$

where the provisional amplitudes $A^{(p)}_{m\mu}$, $A^{(u)}_{m\mu}$ and $A^{(s)}_{m\mu}$ will more than likely not be equal due to the model mismatch. Of course, it is perfectly possible to merely take the average of these amplitudes (not including reflections), but the least-squares method appears to provide a more systematic method by minimising the discontinuities in the variables considered.

We multiply (18) to (20) by r and their respective conjugate basis functions. By integrating across the duct we obtain

$$\sum_{\mu=1}^{M} A^{(p)}_{m\mu} \int_{R_1}^{R_2} \psi_{m\mu}(r)\psi^*_{m\nu} r \, \mathrm{d}r = \int_{R_1}^{R-2} \mathcal{P}_{\omega m0}(r)\psi^*_{m\nu} r \, \mathrm{d}r, \tag{21}$$

$$\sum_{\mu=1}^{M} A^{(u)}_{m\mu} \int_{R_1}^{R_2} \chi_{m\mu}(r)\chi^*_{m\nu} r \, \mathrm{d}r = \int_{R_1}^{R_2} \mathcal{U}_{\omega m0}(r)\chi^*_{m\nu} r \, \mathrm{d}r, \tag{22}$$

$$\sum_{\mu=1}^{M} A^{(s)}_{m\mu} \int_{R_1}^{R_2} \xi_{m\mu}(r)\xi^*_{m\nu} r \, \mathrm{d}r = \int_{R_1}^{R_2} \mathcal{S}_{\omega m0}(r)\xi^*_{m\nu} r \, \mathrm{d}r, \tag{23}$$

or in matrix form,

$$\mathcal{M}\boldsymbol{a}^{(p)} = \boldsymbol{p}, \quad \mathcal{N}\boldsymbol{a}^{(u)} = \boldsymbol{u}, \quad \mathcal{Q}\boldsymbol{a}^{(s)} = \boldsymbol{s}, \tag{24}$$

where

$$\begin{gathered} \{\mathcal{M}\}_{\nu\mu} = \int_{R_1}^{R_2} \psi_{m\mu}(r)\psi^*_{m\nu}(r) r \, \mathrm{d}r, \quad \{\boldsymbol{a}^{(p)}\}_\mu = A^{(p)}_{m\mu}, \\ \{\boldsymbol{p}\}_\nu = \int_{R_1}^{R_2} \mathcal{P}_{\omega m0}(r)\psi^*_{m\nu}(r) r \, \mathrm{d}r, \end{gathered} \tag{25}$$

$$\{\mathcal{N}\}_{\nu\mu} = \int_{R_1}^{R_2} \chi_{m\mu}(r)\,\chi^*_{m\nu}(r) r\,\mathrm{d}r, \quad \{\boldsymbol{a}^{(u)}\}_\mu = A^{(u)}_{m\mu},$$
$$\{\boldsymbol{u}\}_\nu = \int_{R_1}^{R_2} \mathcal{U}_{\omega m0}(r)\,\chi^*_{m\nu}(r) r\,\mathrm{d}r, \tag{26}$$

$$\{\mathcal{Q}\}_{\nu\mu} = \int_{R_1}^{R_2} \xi_{m\mu}(r)\xi^*_{m\nu}(r) r\,\mathrm{d}r, \quad \{\boldsymbol{a}^{(s)}\}_\mu = A^{(s)}_{m\mu},$$
$$\{\boldsymbol{s}\}_\nu = \int_{R_1}^{R_2} \mathcal{S}_{\omega m0}(r)\xi^*_{m\nu}(r) r\,\mathrm{d}r. \tag{27}$$

The least squares approach aims to find a set of amplitudes $\boldsymbol{a}$ that minimizes the cost function

$$c_1 \left\| \mathcal{M}\boldsymbol{a} - \boldsymbol{p} \right\|^2 + c_2 \left\| \mathcal{N}\boldsymbol{a} - \boldsymbol{u} \right\|^2 + c_3 \left\| \mathcal{Q}\boldsymbol{a} - \boldsymbol{s} \right\|^2. \tag{28}$$

The scaling constants

$$c_1 = \frac{1}{p_{\mathrm{ref}}^2}, \quad c_2 = \frac{1}{u_{\mathrm{ref}}^2}, \quad c_3 = \frac{1}{s_{\mathrm{ref}}^2} \tag{29}$$

are necessary because, even though the variables may be non-dimensional, they may not be comparable to one another (because any non-dimensionalisation will be based on the mean flow values). One obvious choice for these scalings is to take $p_{\mathrm{ref}} = \max[\mathcal{P}_{\omega m0}(r)]$, $u_{\mathrm{ref}} = \max[\mathcal{U}_{\omega m0}(r)]$ and $s_{\mathrm{ref}} = \max[\mathcal{S}_{\omega m0}(r)]$.

If we search for the vector $\boldsymbol{a}$ that minimizes the above cost function (28) and use the hermitian property of $\mathcal{M}$, we get* the following equation

$$\left(c_1\mathcal{M}^2 + c_2\mathcal{N}^2 + c_3\mathcal{Q}^2\right)\boldsymbol{a} = c_1\mathcal{M}\,\boldsymbol{p} + c_2\mathcal{N}\,\boldsymbol{u} + c_3\mathcal{Q}\,\boldsymbol{s}, \tag{30}$$

which can be easily solved by standard numerical techniques.

To include the reflected modes in the above analysis is easy: all that is needed is a change of summation limits from

$$\sum_{\mu=1}^{M} \quad \text{to} \quad \sum_{\mu=-M}^{M},$$

(which has a special definition given at the beginning of this section) and to make sure that **at least two variables** are included. The problem remains identical, except that the size of the vectors and matrices are $2M$ and $2M \times 2M$ respectively.

It is interesting to compare this least squares approach with the traditional mode matching method. In traditional mode matching only two variables, pressure p and axial velocity u for instance, are made

*Introduce the complex vectorial inner product $[\boldsymbol{x}, \boldsymbol{y}]$, which is equal to the ordinary inner product with $\boldsymbol{y}$ complex conjugated: $[\boldsymbol{x}, \boldsymbol{y}] = (\boldsymbol{x}, \overline{\boldsymbol{y}})$. Then the hermitian property of $\mathcal{M}$ implies

$$[\mathcal{M}\boldsymbol{x}, \boldsymbol{y}] = [\boldsymbol{x}, \mathcal{M}^*\boldsymbol{y}] = [\boldsymbol{x}, \mathcal{M}\boldsymbol{y}].$$

Each squared distance in the cost function (28) becomes now like

$$\left\| \mathcal{M}\boldsymbol{a} - \boldsymbol{p} \right\|^2 = [\mathcal{M}\boldsymbol{a} - \boldsymbol{p}, \mathcal{M}\boldsymbol{a} - \boldsymbol{p}] = [\mathcal{M}^2\boldsymbol{a}, \boldsymbol{a}] - [\boldsymbol{a}, \mathcal{M}\boldsymbol{p}] - [\mathcal{M}\boldsymbol{p}, \boldsymbol{a}] + [\boldsymbol{p}, \boldsymbol{p}].$$

If we vary around $\boldsymbol{a}$ by substituting $\boldsymbol{a} + \varepsilon\boldsymbol{b}$, we find for $O(\varepsilon)$ that the variation of $\left\| \mathcal{M}\boldsymbol{a} - \boldsymbol{p} \right\|^2$ is

$$2\,\mathrm{Re}\left\{\left[\mathcal{M}^2\boldsymbol{a} - \mathcal{M}\,\boldsymbol{p}, \boldsymbol{b}\right]\right\}.$$

If we look for stationary values of cost function (28) for any vector $\boldsymbol{b}$, the result (30) for $\boldsymbol{a}$ is obtained.

continuous. However with $2M$ unknowns (the transmitted and reflected amplitudes), only $2M$ equations are necessary. In our least squares approach we create even more equations, so that in the case of 2 variables we have $4M$ equations. With only $2M$ unknowns, these equations cannot in general be satisfied exactly and therefore the least-squares solution must be an *approximation*.

It should be noted, however, that unless the basis functions are L_2-orthogonal, the amplitudes found by the traditional method are also an approximation; this concern arises only when we begin to match in a region of a duct with finite-impedance walls. They depend on the number of modes M and on the chosen basis functions used for the inner products. Only when $M \to \infty$ do the amplitudes converge to the (a?) "correct" value.

So in general, the least-squares solution will differ from the traditional mode matching solution. However, as the standard solution produces a small jump across the interface, the least-squares solution (constructed to minimize this jump) will naturally differ only by a small amount.

Further, there is *no* difference when the problem is symmetric and the left- and right-running modes are equivalent. In that case only $2M$ equations are different and the least-squares solution will be equivalent to the traditional mode matching solution (the least squares residue is exactly zero). Because all our current investigations of matching real data occur in hard-walled ducts, we can expect this to be true. In the general asymmetric case, the least-squares solution is expected to produce slightly better results than a direct matching. The inner product equations are more balanced, because there is no dependence on the choice of the basis functions (all, instead of exactly two, can be used).

Since the least squares solution is (a) not restricted to only 2 variables, (b) incorporates very easily any number of continuity conditions and (c) that the formulas, utilizing the hermitian form of the matrices, are very simple, the least squares approach appears to be superior to the traditional approach and worthy of serious consideration.

3.4 Least squares matching across multiple axial planes

Given that the least squares matching is not restricted to two variables, why not use information such as pressure and axial velocity from neighbouring axial planes. In the case where the axial velocity is not *irrotational*, pressure information from n such axial planes can be used as an alternative to a direct matching between pressure and axial pressure gradient. As mentioned before, there is no limit to the number of planes that can be included, but due to the differences in models it would be unwise to employ planes across a wide axial range as this may introduce very large discontinuities that would prove difficult to minimise. For this reason, three axial planes seems to be an ideal choice and we use this number of axial planes in the analysis below. The analysis is easily extended to more than three planes if required.

We start by excluding reflections and assume that we have three axial planes, x_0, x_1 and x_2 with $x_0 < x_1 < x_2$, representing the matching interface. As before, we write the (ω, m) pressure $p_{\omega m}(x, r)$ and axial velocity $u_{\omega m}(x, r)$ components as a sum of their basis functions as follows:

$$p_{\omega m}(x, r) = \sum_{\mu=1}^{M} A_{m\mu}\, \psi_{m\mu}(r)\, \mathrm{e}^{-\mathrm{i}\kappa_{m\mu}(x-x_0)}, \tag{31a}$$

$$u_{\omega m}(x, r) = \sum_{\mu=1}^{M} A_{m\mu}\, \chi_{m\mu}(r)\, \mathrm{e}^{-\mathrm{i}\kappa_{m\mu}(x-x_0)}\,. \tag{31b}$$

Hence, given the Fourier-decomposed pressure and velocity data $\mathcal{P}_{\omega m0}(r)$ and $\mathcal{U}_{\omega m0}(r)$ at $x = x_0$, $\mathcal{P}_{\omega m1}(r)$ and $\mathcal{U}_{\omega m1}(r)$ at $x = x_1$ and $\mathcal{P}_{\omega m2}(r)$ and $\mathcal{U}_{\omega m2}(r)$ at $x = x_2$, we can write

$$\sum_{\mu=1}^{M} A_{m\mu}\psi_{m\mu}(r) = \mathcal{P}_{\omega m0}(r), \tag{32a}$$

$$\sum_{\mu=1}^{M} A_{m\mu}\chi_{m\mu}(r) = \mathcal{U}_{\omega m0}(r), \tag{32b}$$

$$\sum_{\mu=1}^{M} A_{m\mu}\psi_{m\mu}(r)\,\mathrm{e}^{-\mathrm{i}\kappa_{m\mu}(x_1-x_0)} = \mathcal{P}_{\omega m1}(r), \tag{32c}$$

$$\sum_{\mu=1}^{M} A_{m\mu}\chi_{m\mu}(r)\,\mathrm{e}^{-\mathrm{i}\kappa_{m\mu}(x_1-x_0)} = \mathcal{U}_{\omega m1}(r), \tag{32d}$$

$$\sum_{\mu=1}^{M} A_{m\mu}\psi_{m\mu}(r)\,\mathrm{e}^{-\mathrm{i}\kappa_{m\mu}(x_2-x_0)} = \mathcal{P}_{\omega m2}(r), \tag{32e}$$

$$\sum_{\mu=1}^{M} A_{m\mu}\chi_{m\mu}(r)\,\mathrm{e}^{-\mathrm{i}\kappa_{m\mu}(x_2-x_0)} = \mathcal{U}_{\omega m2}(r). \tag{32f}$$

It is now very easy to define new sets of basis functions

$$\zeta_{m\mu}(r) = \psi_{m\mu}(r)\,\mathrm{e}^{-\mathrm{i}\kappa_{m\mu}(x_1-x_0)}, \quad \xi_{m\mu}(r) = \chi_{m\mu}(r)\,\mathrm{e}^{-\mathrm{i}\kappa_{m\mu}(x_1-x_0)},$$
$$\phi_{m\mu}(r) = \psi_{m\mu}(r)\,\mathrm{e}^{-\mathrm{i}\kappa_{m\mu}(x_2-x_0)}, \quad \tau_{m\mu}(r) = \chi_{m\mu}(r)\,\mathrm{e}^{-\mathrm{i}\kappa_{m\mu}(x_2-x_0)},$$

from (32c) to (32f). With these new basis functions, the least-squares procedure can be applied as in the single axial plane case, treating the neighbouring pressure and velocity data as if they were additional flow variables on the same axial plane.

When reflected modes are included in the multi-plane method, some care is needed to prevent exponentially large terms from unbalancing the least-squares minimisation. The diagram in figure 3 shows two pressure modes approaching the three-plane interface from either side. If these modes are cut-off, $\mathrm{Im}(\kappa_{m\mu}) \neq 0$, then their respective amplitudes will decay exponentially as they pass through the interfaces. Hence, if they both have amplitudes of $O(1)$ at the plane x_0, then at $x = x_2$ the amplitude of the right-running cut-off mode will be exponentially small and the amplitude of the left-running mode will be exponentially large. When a multiple axial plane matching method subsequently attempts to resolve both transmitted and reflected modal amplitudes at the same interface, the errors in the cut-off modal amplitudes do not become spread evenly across all the axial planes and the minimisation process becomes unbalanced. A typical effect can be the appearance of large amplitude high-order radial modes that introduce oscillations or "wiggles" into the pressure and velocity profiles reconstructed by the acoustic model. One solution found to the problem is to rescale the left- and right-running amplitudes at whichever axial plane they take their maximum value prior to deriving the matrix equations. In other words, the modes should be rescaled at the axial plane nearest their apparent source. In our diagram for instance, the amplitude of the left-running mode is rescaled to be $O(1)$ at the end interface x_2 and to be exponentially small at $x = x_0$. To demonstrate this rescaling within the context of our analysis, we take

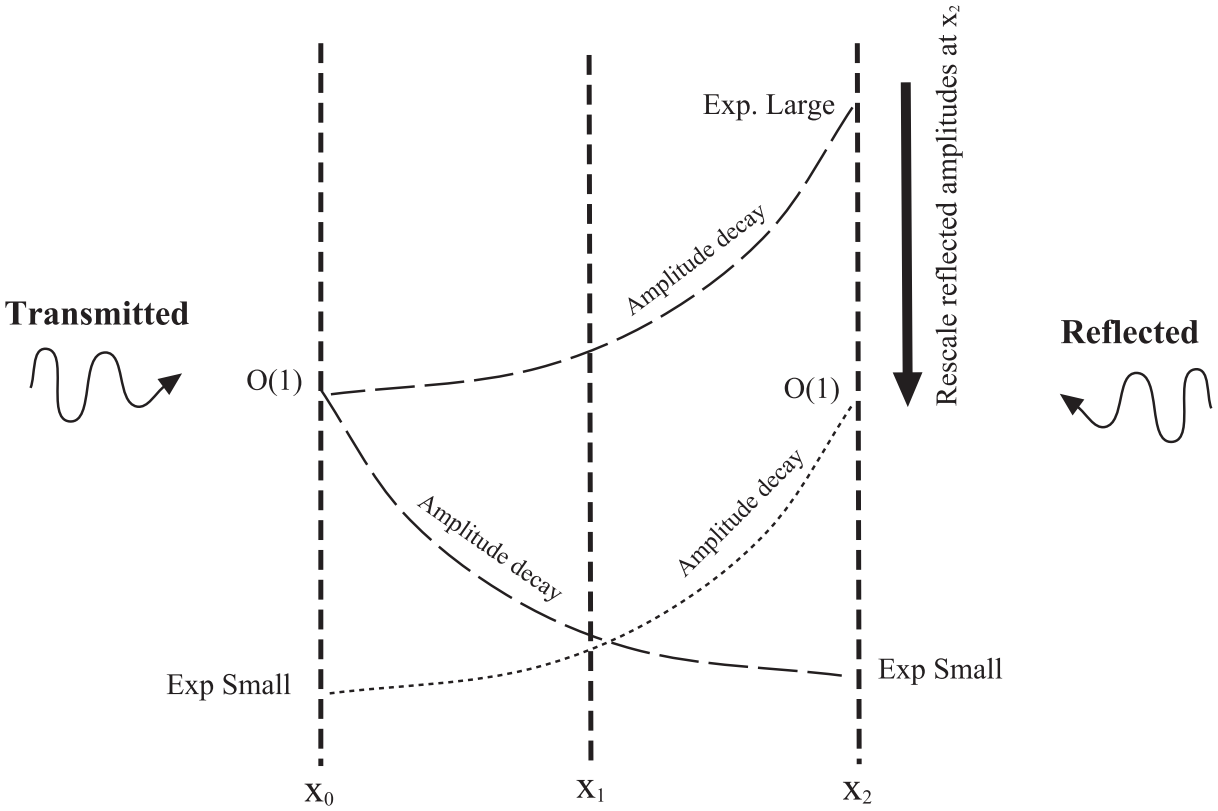

Figure 3: Sketch of the amplitude decay of left- and right-running cut-off modes across three axial planes.

equations (32a) to (32f) as before, but now include the reflected modes in the following way:

$$\sum_{\mu=1}^{M} A_{m\mu}\,\psi_{m\mu}(r) + \sum_{\mu=-M}^{-1} A_{m\mu}\,\psi_{m\mu}(r) = \mathcal{P}_{\omega m0}(r) \tag{33a}$$

$$\sum_{\mu=1}^{M} A_{m\mu}\,\chi_{m\mu}(r) + \sum_{\mu=-M}^{-1} A_{m\mu}\,\chi_{m\mu}(r) = \mathcal{U}_{\omega m0}(r) \tag{33b}$$

$$\sum_{\mu=1}^{M} A_{m\mu}\,\psi_{m\mu}(r)\,\mathrm{e}^{-\mathrm{i}\kappa_{m\mu}(x_1-x_0)} + \sum_{\mu=-M}^{-1} A_{m\mu}\,\psi_{m\mu}(r)\,\mathrm{e}^{-\mathrm{i}\kappa_{m\mu}(x_1-x_0)} = \mathcal{P}_{\omega m1}(r) \tag{33c}$$

$$\sum_{\mu=1}^{M} A_{m\mu}\,\chi_{m\mu}(r)\,\mathrm{e}^{-\mathrm{i}\kappa_{m\mu}(x_1-x_0)} + \sum_{\mu=-M}^{-1} A_{m\mu}\,\chi_{m\mu}(r)\,\mathrm{e}^{-\mathrm{i}\kappa_{m\mu}(x_1-x_0)} = \mathcal{U}_{\omega m1}(r) \tag{33d}$$

$$\sum_{\mu=1}^{M} A_{m\mu}\,\psi_{m\mu}(r)\,\mathrm{e}^{-\mathrm{i}\kappa_{m\mu}(x_2-x_0)} + \sum_{\mu=-M}^{-1} A_{m\mu}\,\psi_{m\mu}(r)\,\mathrm{e}^{-\mathrm{i}\kappa_{m\mu}(x_2-x_0)} = \mathcal{P}_{\omega m2}(r) \tag{33e}$$

$$\sum_{\mu=1}^{M} A_{m\mu}\,\chi_{m\mu}(r)\,\mathrm{e}^{-\mathrm{i}\kappa_{m\mu}(x_2-x_0)} + \sum_{\mu=-M}^{-1} A_{m\mu}\,\chi_{m\mu}(r)\,\mathrm{e}^{-\mathrm{i}\kappa_{m\mu}(x_2-x_0)} = \mathcal{U}_{\omega m2}(r). \tag{33f}$$

Now, for each reflected mode, where $\mu < 0$, we define a rescaled amplitude $B_{m\mu} = A_{m\mu}\,\mathrm{e}^{-\mathrm{i}\kappa_{m\mu}(x_2-x_0)}$,

which shifts the amplitude to represent the magnitude of the reflected mode at the other end of the interface, at $x = x_2$. Consequently, a more balanced system is obtained:

$$\sum_{\mu=1}^{M} A_{m\mu}\psi_{m\mu}(r) + \sum_{\mu=-M}^{-1} B_{m\mu}\psi_{m\mu}(r)\,\mathrm{e}^{-\mathrm{i}\kappa_{m\mu}(x_0-x_2)} = \mathcal{P}_{\omega m0}(r) \tag{34a}$$

$$\sum_{\mu=1}^{M} A_{m\mu}\chi_{m\mu}(r) + \sum_{\mu=-M}^{-1} B_{m\mu}\chi_{m\mu}(r)\,\mathrm{e}^{-\mathrm{i}\kappa_{m\mu}(x_0-x_2)} = \mathcal{U}_{\omega m0}(r) \tag{34b}$$

$$\sum_{\mu=1}^{M} A_{m\mu}\psi_{m\mu}(r)\,\mathrm{e}^{-\mathrm{i}\kappa_{m\mu}(x_1-x_0)} + \sum_{\mu=-M}^{-1} B_{m\mu}\psi_{m\mu}(r)\,\mathrm{e}^{-\mathrm{i}\kappa_{m\mu}(x_1-x_2)} = \mathcal{P}_{\omega m1}(r) \tag{34c}$$

$$\sum_{\mu=1}^{M} A_{m\mu}\chi_{m\mu}(r)\,\mathrm{e}^{-\mathrm{i}\kappa_{m\mu}(x_1-x_0)} + \sum_{\mu=-M}^{-1} B_{m\mu}\chi_{m\mu}(r)\,\mathrm{e}^{-\mathrm{i}\kappa_{m\mu}(x_1-x_2)} = \mathcal{U}_{\omega m1}(r) \tag{34d}$$

$$\sum_{\mu=1}^{M} A_{m\mu}\psi_{m\mu}(r)\,\mathrm{e}^{-\mathrm{i}\kappa_{m\mu}(x_2-x_0)} + \sum_{\mu=-M}^{-1} B_{m\mu}\psi_{m\mu}(r) = \mathcal{P}_{\omega m2}(r) \tag{34e}$$

$$\sum_{\mu=1}^{M} A_{m\mu}\chi_{m\mu}(r)\,\mathrm{e}^{-\mathrm{i}\kappa_{m\mu}(x_2-x_0)} + \sum_{\mu=-M}^{-1} B_{m\mu}\chi_{m\mu}(r) = \mathcal{U}_{\omega m2}(r). \tag{34f}$$

As explained, the basis functions for each set of equations are built from the relevant exponential term multiplied by $\psi_{m\mu}$ or $\chi_{m\mu}$. The least squares method then determines the amplitudes $A_{m\mu}$ for the transmitted waves $\mu > 0$ and $B_{m\mu}$ for the reflected waves $\mu < 0$. The actual reflected amplitudes $A_{m\mu}$ for $\mu < 0$ can be recovered from the resulting $B_{m\mu}$ after the error minimisation is completed.

4 Real and artificial testing of matching procedures

4.1 Introduction

A detailed description concerning our experiences with testing and matching real CFD data onto a simplified acoustic model is now presented. The supplied data comes from three TurboNoiseCFD partners, Rolls-Royce PLC (UK), ONERA (France) and DLR (Germany), and consists of four data sets. Although it is difficult to formulate concrete conclusions from such a small number of test cases, our initial findings reveal some rather interesting and useful observations. Most importantly, the results enable us to propose an optimal strategy to use for the case where the mean flow is nearly uniform with negligible swirl. Further results of the pressure-only matching strategies using artificial test data are also included within this section.

The supplied CFD data must be matched and subsequently entered into a very simple acoustic model. Indeed, the model chosen for our experiments is one of the simplest: a straight circular or annular duct with hard walls and uniform mean flow. In order to achieve a sensible matching, this imposes some loose constraints on the CFD data so that it does not stray too far from the assumptions of the acoustic model. For instance, the data **must not** exhibit large mean swirling flow, highly rotational axial mean flow, finite-impedance walls or severe variations of duct geometry. The matching interfaces of the engine sketch shown in figure 2 most able to adhere to these constraints are the fan-to-inlet-duct interface and, tentatively depending on strength of wakes, the stator-to-bypass-duct interface.

In order to match raw CFD data to an acoustic model, the CFD partners supplying the data have to first perform some post-processing. To test the multi-plane matching strategies, data must be supplied at a minimum of three constant axial planes x_0, x_1 and x_2, with $x_0 < x_1 < x_2$. The total flow field must then be split, on each of these planes, into a steady part (mean flow) and unsteady parts for the frequencies inherent to the problem. This can be achieved via Fourier decomposition in time and circumferential direction (see section 8 for more details of the process,) but note that it is very important to know which **sign** is taken in the Fourier decomposition (especially for the decomposition in time). The mean flow file must contain radial distributions of pressure, the three velocity components, density, temperature, sound speed and entropy; such a large amount of mean flow data enables the acoustic partner to understand the basic assumptions and workings of the CFD model. Then, for each frequency-circumferential (ω, m) mode pair, radial distributions of at least pressure and axial velocity perturbations must be provided in a separate file. It was decided mutually by all the partners to express all values as dimensional quantities both to prevent confusion and to enable correct rescaling of the variables as required for transfer to the acoustic model.

Once the correctly-formatted data files have been produced, the process of matching continues in the following manner. First, the mean flow is stripped of any swirl and any radial variations of the axial mean flow, mean density and mean sound speed are averaged out (whilst conserving mass flux). The quantities are then non-dimensionalised using the simplified mean-flow values: lengths with duct radius, velocities with sound speed, and pressure with the product of mean density and sound speed squared; the mean density and sound speed are consequently normalized to unity.

The matching strategies tested are all based on the methods described in section 3 and are summarized below:

Strategies assuming no reflections

$\mathbf{P}_i$ An option (i) strategy that keeps only pressure continuous across the single axial plane at $x = x_i$. The procedure is repeated at all three axial planes provided and the results from each axial plane x_i can be compared by rescaling each of the resulting modal amplitudes by $e^{-i\kappa_{m\mu}(x_0 - x_i)}$, where $\kappa_{m\mu}$ is the axial wavenumber of the mode, to shift them axially to the origin plane at $x = x_0$.

$\mathbf{PV}_i$ A least-squares strategy based on a single axial plane $x = x_i$ (option iv), where only transmitted modes are assumed and the discontinuity is minimised between pressure and axial velocity data. As the single pressure matching above, this method is also applied to all three axial planes x_0, x_1 and x_2 and scaled accordingly to enable a comparison to be made.

P∇P A least-squares strategy applied at the middle axial plane (option iv). It is similar to **$\mathbf{PV}_i$** above, but here the axial velocity is replaced with an axial pressure gradient derived from the pressure data at the two outer axial planes. The amplitude is shifted to the origin plane $x = x_0$ for comparison using the procedure described above.

3P A multi-plane strategy (option v) that performs a least-square minimisation of the pressure data at all three axial planes **excluding reflected modes**.

3P+3V A multi-plane strategy (option v) that performs a least-square minimisation of both pressure and axial velocity data at all three axial planes **excluding reflected modes**.

Strategies that include reflections

(P+V)$_i$ The option (ii) strategy that keeps both pressure and axial velocity continuous across the single axial plane at $x = x_i$. The method is applied to all three interfaces and the modal amplitudes are shifted axially (as described above) for comparison.

P+∇P The option (iii) strategy where both the pressure and the axial pressure gradient are kept continuous across a single axial plane. The axial pressure gradient is determined numerically at the middle axial plane using the pressure information from the outer axial planes. This method is applied at the middle axial plane only and the amplitude is then shifted axially to the origin plane $x = x_0$ using the procedure described previously.

All-P A multi-plane strategy (option v) that performs a least-square minimisation of the pressure data at all three axial planes and includes both transmitted and reflected modes.

All-P+V A multi-plane strategy (option v) that performs a least-squares minimisation of both pressure and axial velocity data at all three axial planes including both transmitted and reflected modes.

4.2 Myers's definition of acoustic energy

The matching process aims to transfer the sound produced by the source region (and calculated by the CFD model) to a simpler acoustic model without generating sources or sinks at the model discontinuity. In other words, it would be ideal to somehow conserve the *acoustic energy* during the transfer. However, acoustic energy is not an easy concept to define as it represents second-order quantities within the energy of the entire flow field. In general flow fields, total energy is conserved but "acoustic energy" (in one form of definition or another) remains coupled to the leading- (zero-) order mean flow energy. Interactions between mean and perturbed flow can subsequently augment or dampen the sound level. In relatively special cases, however, where the flow field is isentropic and irrotational, can a conserved acoustic energy be defined.

Following the work of Cantrell and Hart [10] and Morfey [11], a formulation developed by Myers [12] attempts to create a more general acoustic energy conservation law assuming only homentropicity (in other words, d$s = 0$, where s is the entropy); the formulation has been further developed in [13]. His definition adopts the position that vorticity is non-acoustic and embodies both sources and sinks of acoustic energy. According to Myers, the time-averaged acoustic energy flux (a second-order quantity) can be written as

$$\boldsymbol{I} = (\rho_0 \boldsymbol{v}' + \rho' \boldsymbol{v}_0) \left(\frac{{c_0}^2 \rho'}{\rho_0} + \boldsymbol{v}_0 \cdot \boldsymbol{v}' \right), \tag{35}$$

where ρ_0 and $\boldsymbol{v}_0$ are the mean density and mean velocity and ρ' and $\boldsymbol{v}'$ are the density and velocity perturbations respectively.

In the data sets examined in sections 4.5, 4.6 and 4.7, Myers's time-averaged acoustic energy flux is integrated over each axial plane for both raw CFD and modal data (in the case of the modal data, the energy flux is actually conserved due to the assumption of uniform mean flow); the raw data calculation uses the original mean flow data with out any alterations. Comparisons of these energy fluxes between neighbouring interfaces and between the CFD and modal data reveal some remarkable observations about sound propagation in non-uniform mean flows.

4.3 CAA Benchmark Case (Rolls-Royce)

Description of data

The first data set supplied by Rolls-Royce plc comes from a category 4 benchmark problem from the 3rd Computational Aeroacoustics Workshop on Benchmark Problems (Cleveland, OH, USA, 8-10 November 1999). The problem consists of a set of sixteen vortical wakes impinging on a set of twenty four flat aligned (and thus unloaded) stator vanes in a parallel annular duct with uniform axial mean flow. A full description of the problem and the numerical results are presented by Wilson [14]. Data was provided for both 1D non-reflecting boundary conditions and improved 3D non-reflecting boundary conditions. Only information from the latter was matched because of its greater accuracy. Six axial planes (three upstream and three downstream) and four circumferential modes were included (m=-32,-8, 16 and 40) for a single frequency with Helmholtz number $\omega = 12.532$. The three axial planes upstream are positioned at $x_0 = -0.125$m, $x_1 = -0.122$m and $x_2 = -0.119$m and the three axial planes downstream are positioned at $x_3 = 0.219$m, $x_4 = 0.222$m and $x_5 = 0.225$m, relative to the stator vanes. The axial mean flow Mach number is 0.5 and the hub-to-tip ratio is also 0.5.

General observations

The wavesplitting carried out by Rolls-Royce (in part to assist our assessment of the matching strategies) suggested that, out of the four circumferential modes supplied, only the $m = -8$ case would yield interpretable results. The other circumferential modes do not have any cut-on modes, which propagate away from the area of the source, and as the axial planes are located far from the sound source, the magnitudes of the cut-off modes are very small and similar in size to the magnitude of the spurious reflections. At present, we are not certain whether these reflections and outgoing cut-off modes are comparable to the inherent errors of the numerical procedure or a mere by-product of the applied outgoing boundary condition (or indeed both). We concluded that it was realistically impossible to determine the amplitudes of the cut-off modes accurately and thus concentrated our efforts on determining the amplitudes of the two cut-on modes occurring in the $m = -8$ case.

In performing the matching, we noticed that the method of using more than a single axial plane can be of great benefit in checking consistency and accuracy. A clear example is apparent in the current data set, where by comparing the modal amplitudes given by both the $\mathbf{P_i}$ method at each interface and by the **3P** and **All-P** matchings we are able to determine how Rolls-Royce had Fourier decomposed their data. When the incorrect sign convention is taken in the time decomposition, larger phase differences are observed between the amplitudes determined from the single pressure methods at each axial plane and, consequently, the multi-plane pressure matchings give absurd results. Without using a multi-plane matching strategy, it would not have been possible to tell whether our sign convention was the same one used by Rolls-Royce. Changing to the correct sign is fairly straightforward, as only the complex conjugate of the post-processed CFD data need be taken.

Every matching strategy enables the user to choose how many modes are included, but the inclusion of more cut-off modes *does not* necessarily guarantee a better matching (although it doesn't become worse either, at least in our case). As higher and higher radial modes are included, the reconstructed pressure and velocity profiles begin to exhibit strong 'wiggles' in the neighbourhood of the inner cylinder, particularly in matching strategies where both axial velocity and pressure are used. For multi-plane strategies, some 'wiggles' can be suppressed by balancing the left- and right-running modal amplitudes correctly for the cut-off modes in the least-squares procedure (see section 3.4 for details). In other cases,

the error appears close to the inner cylinder, probably because our least-squares methods minimise in the L_2-norm as opposed to the sup-norm. Despite the appearance of wiggles, increasing the number of cut-off modes does not alter the amplitudes of the lower-order modes in any way. We would expect this to be true due to the orthogonality of the hard-wall modes and so we can be confident that not many radial modes need to be taken in this particular case to model the sound field. However, the effect may be a problem when an interface lies in a region of the duct with soft-walls, where the non-orthogonality of the modes may necessitate a large number of radial modes for uniqueness.

The inlet: upstream of the stator vanes

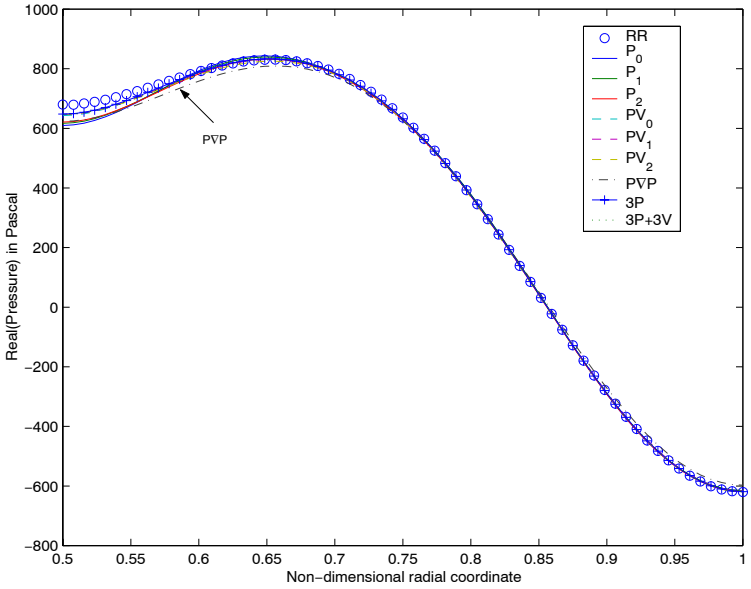

Figure 4: Reconstructed unsteady inlet pressure profiles (real part) for matching strategies assuming no reflections.

Perhaps the most important observation one can make about the matching upstream of the stator vanes is that every matching strategy performed very well. This can be seen in the figures 4 and 5, which show the real parts of the reconstructed pressure profiles at one axial plane generated by each matching strategy and plotted against the original data from Rolls-Royce. Figure 4 shows the profiles from strategies **not** including reflections and figure 5 shows the profiles from strategies that included reflections.

The following positive conclusions can be drawn from this result. First, it is clear that reflections are not very significant; the improvement to the curve fit in figure 5 compared to figure 4 is only very slight. The derived reflected amplitudes are all less then 1% of the magnitude of the cut-on transmitted amplitudes indicating that the 3D non-reflecting boundary condition appears to work very well. Second, the matching strategies that use axial velocity information perform equally as well as the ones that do not. Hence, the flow has remained irrotational upstream as expected.

The excellent agreement between the results also indicates that the more novel least-squares and multi-plane approaches are able to produce consistent results. However, out of the strategies that include reflections, the **All-P** method suggested that the amplitude of these reflections were much higher (about 1% of the transmitted amplitude of the cut-on modes) than the other strategies which use axial velocity

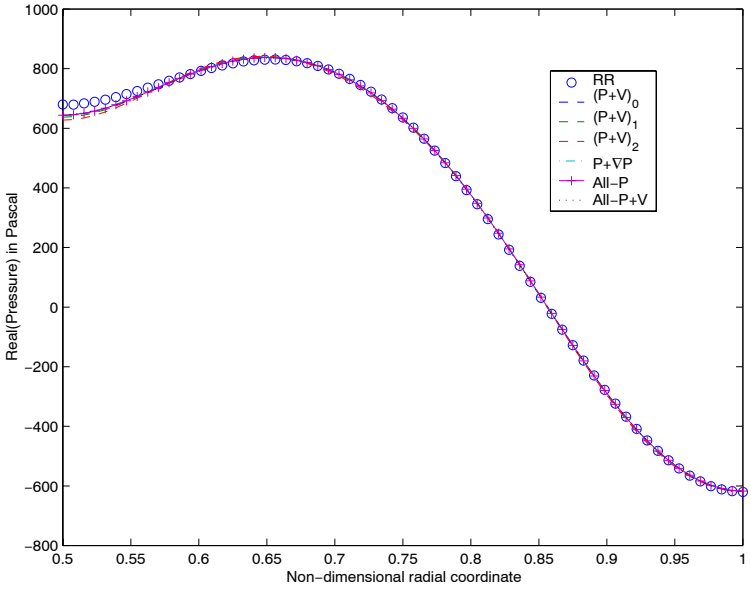

Figure 5: Reconstructed unsteady inlet pressure profiles (real part) for matching strategies that include reflections.

information (reflected amplitudes of about 0.1% of the transmitted amplitudes). Which one is more accurate? This is impossible to tell from one set of data, especially as in both cases the reflected amplitudes seem to lie within the inherent errors of the numerics. One concern is that the lack of orthogonality between the three pressure distributions at neighbouring axial stations may be the cause. To determine directional information, it is the small differences in pressure that are required and possibly these are not accentuated enough in the **All-P** method. However, it is also highly likely that the method of wave splitting and thus suppressing reflections involves axial velocity data, which would, in turn, mean lower reflections in any matching strategies using axial velocity. The issue prompted us to perform some artificial testing, presented in the next section, to investigate the ability of the **All-P** matching method to determine the directional behaviour of modes compared to a strategy using a derived pressure gradient. As we will see in the next section, the results of the artificial tests more or less vindicate the **All-P** method and we must look to the latter reason or some other feature of the CFD model to explain this anomaly.

The exhaust: downstream of the stator vanes

Contrary to the results at the inlet, it is clear that the axial velocity has a **significant vortical part** downstream and cannot be applied successfully to any matching strategy. In other words, the downstream wakes of the stator vanes are highly vortical (even for unloaded axially aligned stator vanes) and, as the acoustical information is only stored within the solenoidal component of the velocity, it cannot in this case be extracted directly from the velocity data.

The evidence for the conclusion above can be seen in the plots of the reconstructed pressure profiles from each matching strategy at one of the axial planes (figures 6 and 7). When reflections are not included, all of the matching strategies that use axial velocity data fail to recreate the original pressure profile. In the methods where reflections are included, only the $(\mathbf{P}+\mathbf{V})_5$ direct matching strategy, which uses the data of the axial plane where the pressure profile is compared, recreates the profile exactly (as required

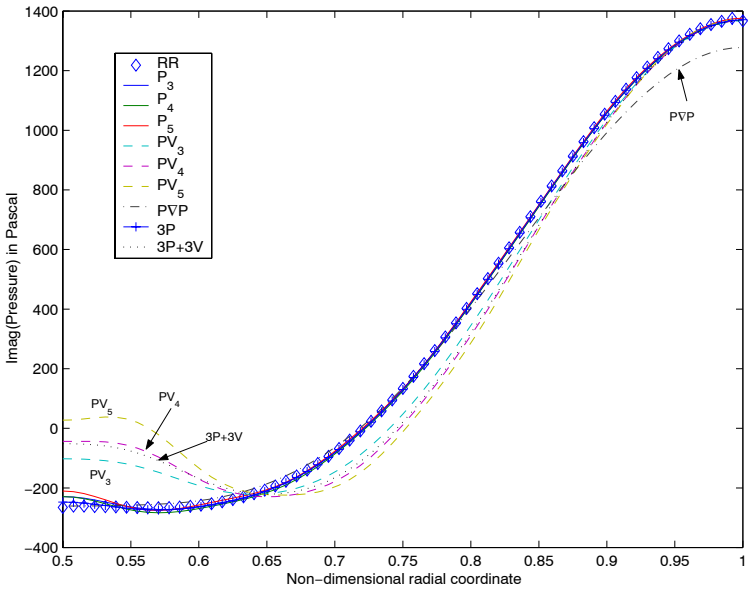

Figure 6: Reconstructed unsteady exhaust pressure profiles (imag part) for matching strategies assuming no reflections.

because the option (ii) strategy requires pressure and axial velocity to be continuous). However, the same direct method applied to data at the two neighbouring interfaces and plotted as $(\mathbf{P}+\mathbf{V})_3$ and $(\mathbf{P}+\mathbf{V})_4$ is unable to reproduce the plotted pressure profile. Compare this to the results of the $\mathbf{P_3}$, $\mathbf{P_4}$ and $\mathbf{P_5}$ methods in figure 6, which successfully agree with one another (and the original CFD profile) at the same interface. Strong vorticity contamination is the only explanation.

With the above points in mind, in a situation where the axial velocity is strongly contaminated (or expected to be) one is forced to rely on matching strategies that use pressure information **only**. Therefore, to include and/or perhaps verify that reflections are small we need to apply either a triple-plane pressure matching strategy such as **All-P** or derive a numerical pressure gradient and use a direct traditional matching method such as $\mathbf{P}+\nabla\mathbf{P}$. Which of these options is preferable cannot be determined from these results alone and some testing of artificial data presented in the next section is necessary to shed some light on the issue.

4.4 Testing with artificially generated data

An investigation was undertaken principally to discover how robust the pressure-only matching strategies that include reflections are. The question arising from the CAA benchmark case analysis was: given three axial planes with radial pressure distributions (for a particular frequency and circumferential wavenumber), is it better to perform a least-squares minimisation with the three pressure distributions (the **All-P** method) or to derive an axial pressure gradient and perform a direct matching with the pressure at the middle axial plane (the $\mathbf{P}+\nabla\mathbf{P}$ method)? The artificial testing consisted of building test profiles by summing known modal basis functions with random amplitudes (and if required adding some degree of noise) and then applying the two matching strategies with varying distances between the axial planes and varying other grid properties.

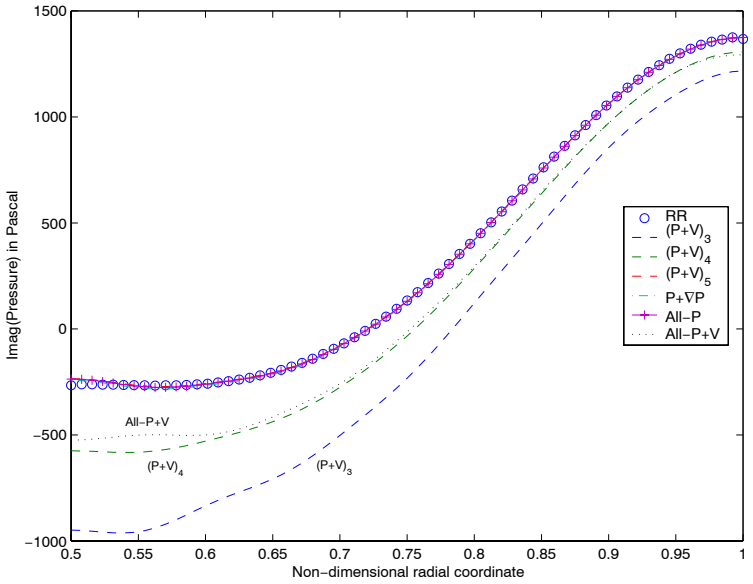

Figure 7: Reconstructed unsteady exhaust pressure profiles (imag part) for matching strategies that include reflections.

The results of testing the effect of spacing between the axial planes revealed that a derived pressure gradient, which uses pressure data at the two outer axial planes to derive an axial pressure gradient at the middle plane, is **highly sensitive** to the spacing between the planes. For non-dimensional spacings (scaled on the duct radius) below 10^{-2} the errors become unacceptable and when the spaces between the planes are uneven the errors become worse. In fact, the **All-P** matching strategy **outperforms** the $\mathbf{P} + \nabla\mathbf{P}$ matching strategy over the entire range of interface spacings, from large uneven spacings to tiny non-dimensional spacings of $O(10^{-7})$. As we had previously speculated that directional information may be difficult to extract from the **All-P** method (see the previous section), this result turned out to be a real surprise.

Not only did the artificial test confirm the **All-P** method as insensitive to the distance between axial planes, but it also helped improve the method by highlighting the need to carefully balance the determination of left- and right-running cut-off modes across multiple axial planes (see section 3.4 for a detailed description).

We observed in the tests that, for any matching strategy including reflections, the largest error in amplitude nearly always occurs in the radial mode closest to cut-on cut-off transition. In the CAA benchmark case matching of the previous section, a similar phenomenon could also be observed and there appears to be an obvious explanation. For a radial mode near transition, the axial wavenumbers $\kappa_{m\mu}$ for the left- and right-running components (in the hard-wall case) are almost equal and, consequently, the basis functions for pressure, $\psi_{m\mu}$, and axial velocity, $\chi_{m\mu}$, of the two components are almost nearly equal; refer to the expressions given by equations (12) and (13) for our uniform flow case. Therefore, there is a lack of directionality in modes near transition (the mode is almost at resonance) and numerically resolving the transmitted and reflected amplitudes will inevitably be more difficult.

Finally, the effect of varying the number of radial points supplied in the raw data was tested and a rather remarkable observation was noted. When only a modest number of radial points is supplied by the CFD partner, the accuracy of the derived modal amplitudes for the lower-order radial modes can be signif-

icantly improved by splining the data (in other words, by assuming it is smooth) and then performing the radial decomposition on a finer grid. In one particular example of artificial data contaminated with a small amount of random noise, an error of 20% in the amplitude of the first-order radial cut-on mode was reduced to less then 1% by this procedure.

4.5 FANPAC test case of rotor alone noise (ONERA)

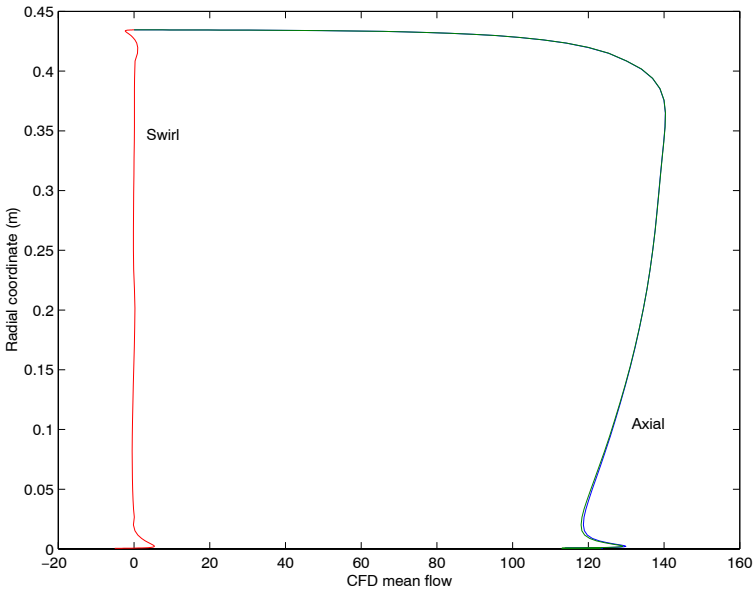

Figure 8: FANPAC test case: axial and azimuthal mean flow upstream.

Description of data

The data supplied by ONERA comes from a Workpackage 1.3 FANPAC test case to investigate rotor alone noise. The geometry is a parallel cylindrical duct containing a fan (no stator) with 24 rotor blades. Although the actual duct is hollow, the CFD results contain a very small annulus (needed for their model). The mean flow can almost be taken as axial and uniform (see figure 8), but note the appearance of sizable boundary layers particularly on the fictitious annulus. The outer radius of the duct is 0.435m and the data set consists of three axial planes lying at 0.618m, 0.620m and 0.622m upstream of the rotor. The blade passing frequency (BPF) is given as 3233Hz and three sets of unsteady data in circumferential (m-) mode - frequency pairs were provided: (i) $m = 24$ at 1BPF, (ii) $m = 48$ at 2BPF and (iii) $m = 72$ at 3BPF.

Results of matching

For this real data analysis, the matching strategies were performed on all three circumferential mode frequency pairs and the time-averaged acoustic energy flux (non-dimensional, see section 4.2) was calculated across each axial plane for the raw CFD data, and at a chosen axial plane for each matching strategy. The non-dimensional values are shown in tables 1 to 3. Figures 9 to 11 also present real and/or

Table 1: Time-averaged acoustic energy flux measurements (axial): m=24, 1BPF case

Raw CFD data	
X	Value
0.618	-0.699 E-5
0.620	-0.703 E-5
0.622	-0.696 E-5

Strategies that include reflections				
$(P+V)_{618}$	$(P+V)_{620}$	$(P+V)_{622}$	All P	All $P+V$
-0.647 E -5	-0.646 E-5	-0.633 E-5	-0.616 E-5	-0.640 E-5

Strategies assuming no reflections							
P_{618}	P_{620}	P_{622}	PV_{618}	PV_{620}	PV_{622}	$3P$	$3P+3V$
-0.533E-5	-0.618E-5	-0.707E-5	-0.569E-5	-0.650E-5	-0.731E-5	-0.609E-5	-0.641E-5

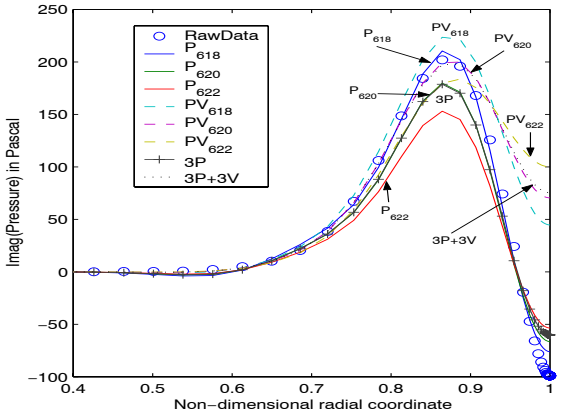

(a) Imag(Pressure): assuming no reflections.

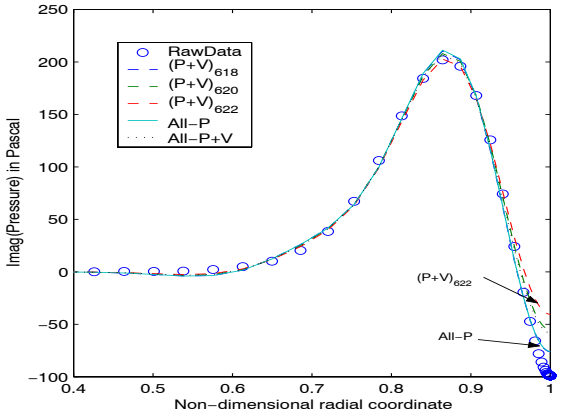

(b) Imag(Pressure): including reflections.

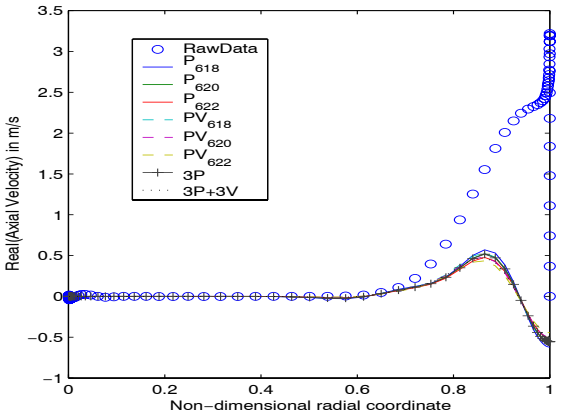

(c) Real(Axial Vel.): assuming no reflections.

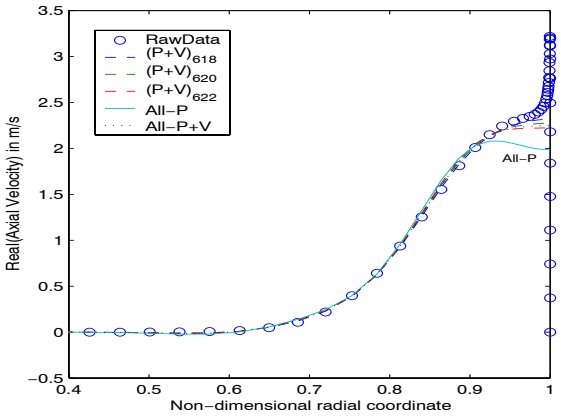

(d) Real(Axial Vel.): including reflections.

Figure 9: Reconstructed unsteady pressure and unsteady axial velocity profiles for m=24, 1BPF case.

Table 2: Time-averaged acoustic energy flux measurements (axial): m=48, 2BPF case

Raw CFD data	
X	Value
0.618	-0.316 E-5
0.620	-0.337 E-5
0.622	-0.342 E-5

Strategies that include reflections				
$(P+V)_{618}$	$(P+V)_{620}$	$(P+V)_{622}$	All P	All $P+V$
-0.289 E -5	-0.315 E-5	-0.325 E-5	-0.309 E-5	-0.312 E-5

Strategies assuming no reflections							
P_{618}	P_{620}	P_{622}	PV_{618}	PV_{620}	PV_{622}	$3P$	$3P+3V$
-0.386E-5	-0.346E-5	-0.294E-5	-0.340E-5	-0.326E-5	-0.295E-5	-0.338E-5	-0.319E-5

imaginary parts of reconstructed pressure and axial velocity profiles for each matching strategy, plotted against the original CFD-supplied profile.

Once again (as in the CAA Benchmark case), the matching across multiple axial planes enables us to determine whether the correct sign convention has been taken for the Fourier decomposition in time. In addition to the modal behaviour already noted previously, the choice of sign convention has a prominent effect on the time-averaged acoustic energy fluxes calculated from the multi-plane **All-P** and **All-P+V** matching methods. When the incorrect sign is taken, these fluxes do not appear consistent with the time-averaged acoustic energy fluxes determined from the raw CFD data and other matching methods. In many instances, the multi-plane strategies give time-averaged acoustic energy fluxes that do not even appear physically possible, having the wrong sign and, hence, the wrong direction of propagation for example.

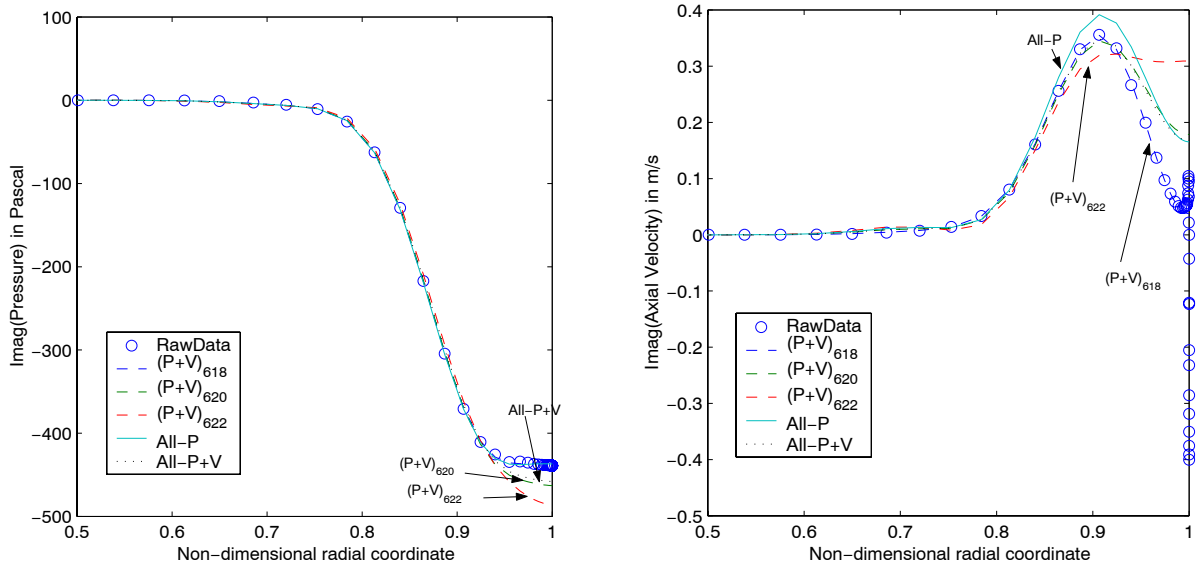

(a) Imag(Pressure): including reflections.

(b) Imag(Axial Vel.): including reflections.

Figure 10: Reconstructed unsteady pressure and unsteady axial velocity profiles for m=48, 2BPF case.

Table 3: Time-averaged acoustic energy flux measurements (axial): m=72, 3BPF case

Raw CFD data	
X	Value
0.618	-0.490 E-6
0.620	-0.550 E-6
0.622	-0.556 E-6

Strategies that include reflections				
$(P+V)_{618}$	$(P+V)_{620}$	$(P+V)_{622}$	All P	All $P+V$
-0.364 E-6	-0.420 E-6	-0.436 E-6	-0.359 E-6	-0.393 E-6

Strategies assuming no reflections							
P_{618}	P_{620}	P_{622}	PV_{618}	PV_{620}	PV_{622}	$3P$	$3P+3V$
-1.297E-6	-1.428E-6	-1.408E-6	-0.875E-6	-0.959E-6	-0.956E-6	-1.355E-6	-0.922E-6

In contrast to the first set of Rolls-Royce data in section 4.3, it is reflected modes that are now the main problem (as opposed to vorticity). Compare the reconstructed pressure profiles in figure 9 for strategies including reflections and assuming no reflections. For the $m = 24$ and $m = 72$ cases the reflected amplitude of the first cut-on mode is predicted by the various matching strategies to be half the amplitude of the transmitted component. For $m = 48$ the reflected amplitude is closer to 30% of the transmitted amplitude.

As expected upstream of the rotor, the vorticity is not so significant and, for this reason, all of the matching strategies including reflections predict the pressure and axial velocity accurately at all three axial planes. Errors occur close to the outer wall but these are attributed to the presence of vorticity in the boundary layer. The fictitious annulus does not appear to have any direct impact on the results, although this may be more due to the fact that very large values of m have been chosen (the inner geometry

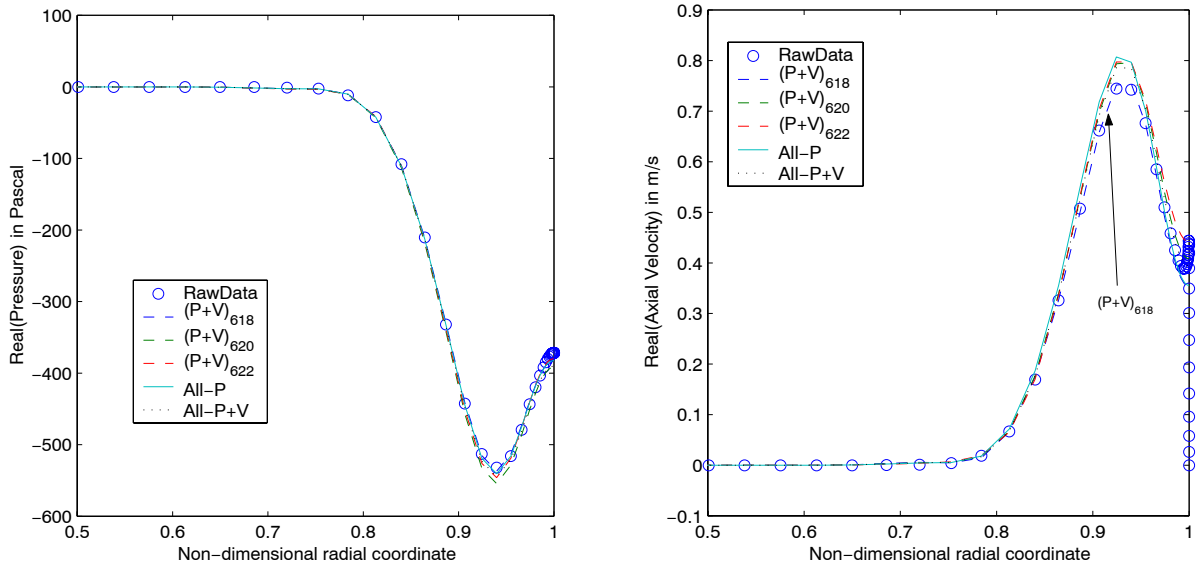

(a) Real(Pressure): including reflections.

(b) Real(Axial Vel.): including reflections.

Figure 11: Reconstructed unsteady pressure and unsteady axial velocity profiles for m=72, 3BPF case.

becomes less significant in this case). The multiple-plane strategies that include reflections, **All-P** and **All-P+V**, perform well by averaging out the numerical discrepancies between the axial planes to produce an excellent representation of the perturbed flow field, especially outside the outer-wall boundary layer.

The absence of vorticity in the flow field, and the consequent lack of coupling between vortical and acoustic fields can be confirmed by the reasonable agreement in time-averaged acoustic energy flux between the raw CFD data and modal representations (tables 1-3). The importance of including reflections is highlighted in the $m = 72$ case in table 3, where the strategies excluding reflections estimate the acoustic energy flux to be more than double the CFD value in all cases. However, perhaps just as remarkable is the reasonable prediction of acoustic energy flux given in the other circumferential mode cases when reflections are excluded. Other minor discrepancies in the energy flux prediction (of the order of 10%) are most likely caused by the boundary layers.

4.6 RESOUND Fan/OGV test case in the bypass duct (Rolls-Royce)

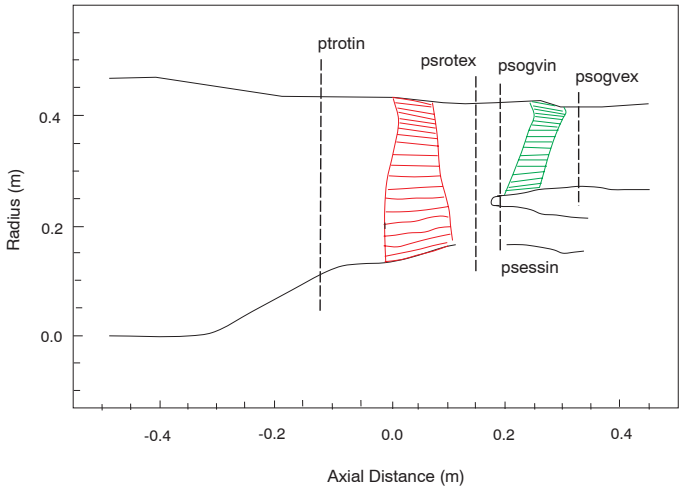

Figure 12: Fan/OGV RESOUND testcase geometry. Rolls-Royce supplied ten axial planes located at the stator-to-bypass-duct interface (psogvex). The duct has hard walls.

Description of data

The second set of Rolls-Royce test data is based on a more realistic situation using a RESOUND testcase geometry (figure 12) for investigating noise generated by rotor/stator interaction. Clearly, the engine duct geometry varies significantly along its axis, but in the region of the duct behind the stator (psogvex), the duct is more or less parallel, with radial variations of $O(10^{-4}\text{m})$, and so our matching strategies can be applied directly. Rolls-Royce supplied CFD data at ten axial planes equally spaced between $x = 0.320$m and $x = 0.360$m for the stator-to-bypass-duct interface. Perturbation data was provided for a single frequency, with a Helmholtz number based on the outer duct radius of 40.89 (2BPF), and single circumferential wavenumber, $m = -13$. Observe in figure 13 that the mean flow has hardly any swirl but contains vorticity (as expected). Stripping this mean flow to create a simple uniform flow leads to a

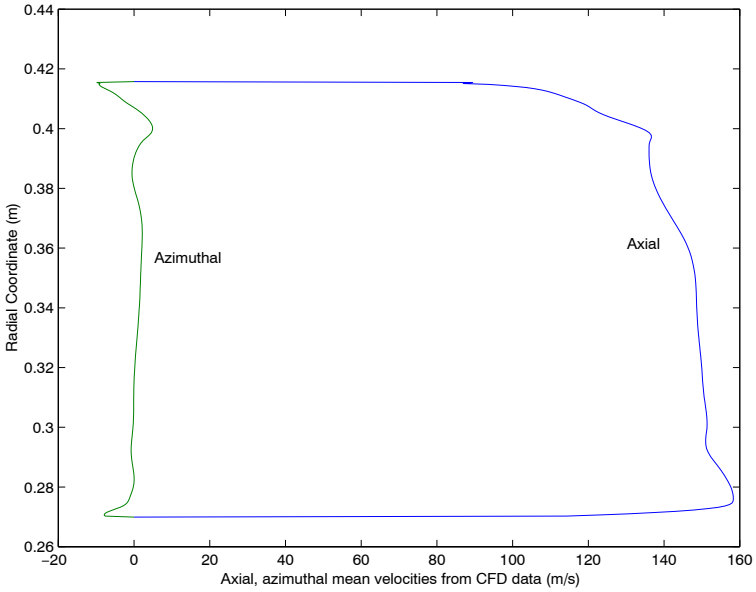

Figure 13: Rolls-Royce's Fan/OGV RESOUND testcase. Axial and azimuthal CFD mean flow profiles at $x = 0.340$m.

mean axial Mach number of $M = 0.44$ and the average hub-to-tip ratio across the interfaces is 0.649. Solving the eigenvalue problem for the acoustic model predicts five cut-on radial modes in this case.

Results

The matching strategies were applied across all ten axial planes and unsteady pressure and axial velocity profiles were reconstructed from the modal solutions. The axial time-averaged acoustic energy flux of the raw CFD data (using Myers's definition from section 4.2) and the derived time-averaged acoustic energy fluxes from each of the matching methods were also computed at each axial plane. The main observations made are described below.

On performing the matchings, it soon became clear that there is significant vorticity contamination and just as significant reflections in this case. The results of matching from methods assuming no reflections can be quickly discounted as they fail to represent the flow field in any way. The **All-P** method indicates that the reflected amplitudes of the cut-on modes are about 20% of the amplitude of their transmitted counterparts. These two effects combined made it incredibly difficult even to judge the sign convention of the Fourier time decomposition from the modal amplitudes given by each strategy. The sign convention was eventually chosen to be the one with the most sensible time-averaged acoustic energy flux and the smallest residue for the **All-P** method. As seen in the ONERA data, taking the incorrect sign convention often produces an absurd value for the acoustic energy flux (or so it would seem), which may even indicate the overall acoustic energy propagating towards instead of away from the source.

The strength of the vortical part of the flow field compared to the irrotational acoustical part can be clearly seen in the reconstructed axial velocity profiles, taken at one of the interfacial axial planes and presented in figure 14. The most striking observation one can make from the profiles is that the strategies using all the pressure data available predict, and hence support, only (irrotational) velocity perturbations of approximately one tenth of the magnitude of the ones observed. The three $(\mathbf{P}+\mathbf{V})_i$ direct matching

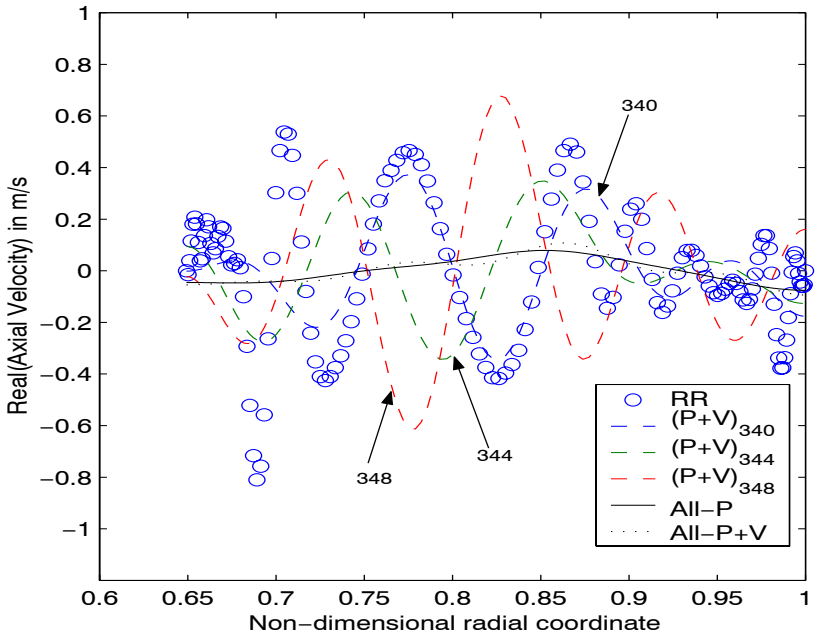

(a) Real Part: Unsteady Axial Velocity Component

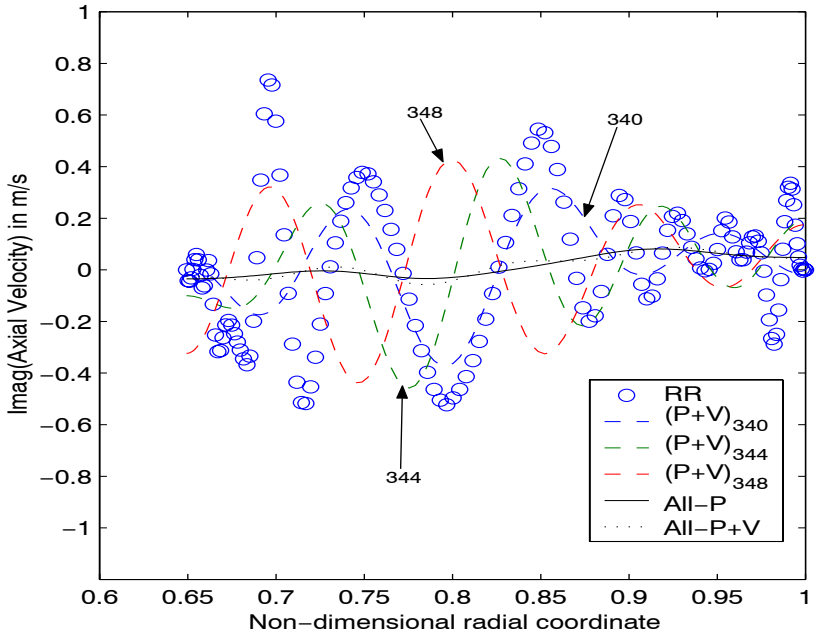

(b) Imag Part: Unsteady Axial Velocity Component

Figure 14: Reconstructed unsteady axial velocity profiles at one of the *matched* axial planes, $x = 0.340$m, for matching strategies that include reflections.

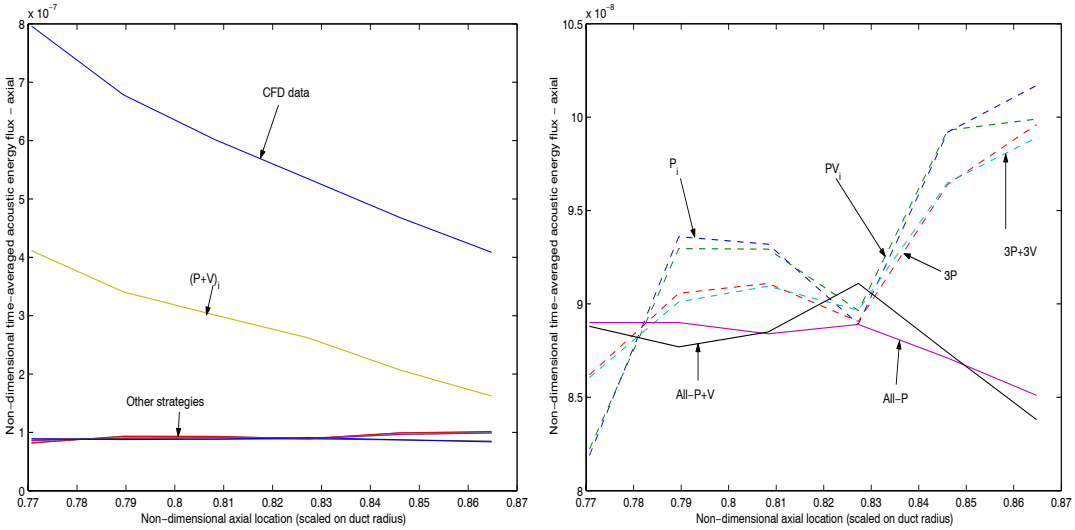

(a) Raw CFD and modal solutions

(b) Close up of other matching strategies.

Figure 15: Plotted values of the time-averaged acoustic energy flux (axial) for both the raw CFD data and the modal solutions across all ten supplied axial planes.

methods, determined at each neighbouring axial plane, attempt to fit the CFD data assuming a solenoidal velocity field but, as the largest component of the velocity field is vortical, the results from $(\mathbf{P}+\mathbf{V})_{\mathbf{340}}$, $(\mathbf{P}+\mathbf{V})_{\mathbf{344}}$ and $(\mathbf{P}+\mathbf{V})_{\mathbf{348}}$ (determined from the data at $x = 0.340$m, $x = 0.344$m and $x = 0.348$m respectively) disagree completely with one another when compared at the same axial plane (at $x = 0.340$m).

The observation that the vortical part of the axial velocity perturbations is greater than the solenoidal part is also borne out in the calculations of the axial time-averaged acoustic energy flux presented in figure 15. Comparing the values for the raw CFD data to those derived from each matching strategy, one can clearly observe that the original CFD flow field has roughly ten times the time-averaged acoustic energy flux of the modal profiles. The only exception to this rule is the direct $(\mathbf{P}+\mathbf{V})_{\mathbf{i}}$ method, which treats the axial velocity at the single axial plane as being completely irrotational, and this method achieves an acoustic energy flux about half that of the raw CFD data. Compare the similar differences observed in the reconstructed axial velocity profiles in figure 14. An even stranger phenomenon is the way the axial time-averaged acoustic energy flux for the raw CFD data falls sharply away from the source, although the duct itself and the mean flow exhibit no axial variation. This interesting observation must be created via a coupling between vortical and acoustic modes (possibly via the hydrodynamic cut-off modes as they have strong axial variation) and raises some interesting questions to answer in any future research. Equally intriguing is why the derived acoustic energy fluxes for each of the matching strategies, except $(\mathbf{P}+\mathbf{V})_{\mathbf{i}}$ but particularly the multi-plane methods including reflections, remain relatively constant across the ten axial planes supplied. On the one hand, an almost constant value may seem to make sense, because the simple acoustic model conserves acoustic energy, but on the other hand the information comes from the raw CFD data where the acoustic energy should not be (and is not) conserved.

These experiences with Myers's acoustic energy definition suggest that without better understanding of *acoustic energy*, the current definition cannot be incorporated directly into an optimal matching strategy (such as one that minimises the discontinuity in the energy across the interface), but used merely as an additional guide. With our present knowledge, the pressure field must be taken as a more reliable

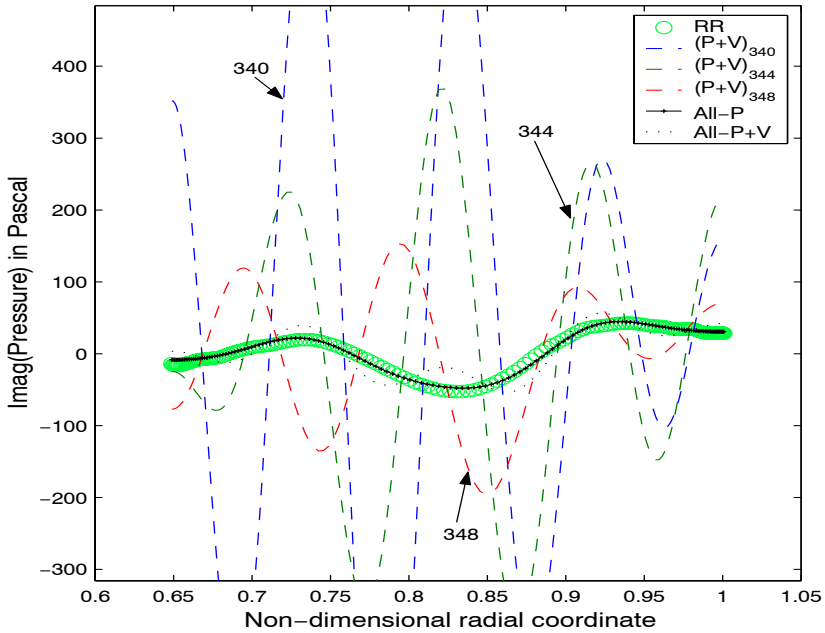

(a) Imag Part: Unsteady Pressure Component

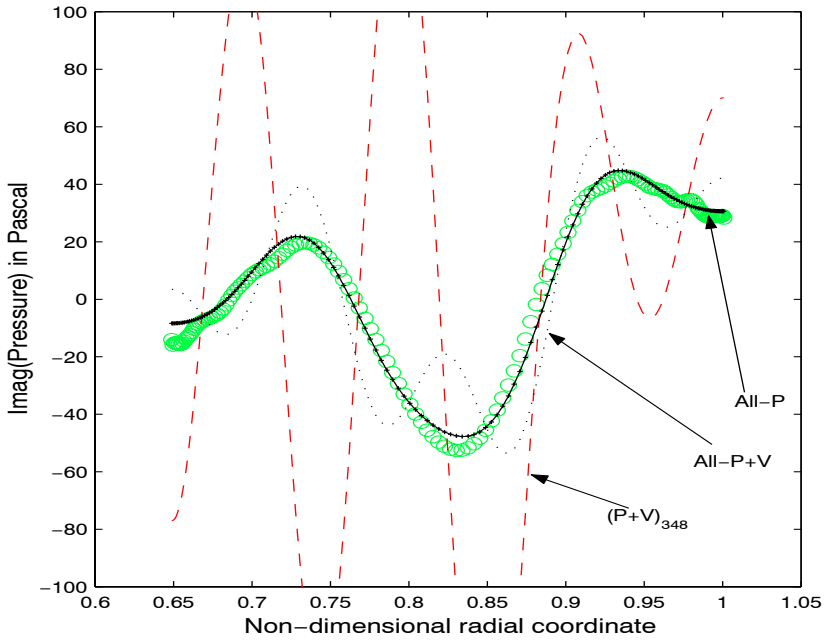

(b) Imag Part: Unsteady Pressure Component (magnified)

Figure 16: Recreating a pressure profile downstream of the interface using the matching strategies that include reflections. Here, the interface is taken as the three axial planes at $x = 0.340$m, $x = 0.344$m and $x = 0.348$m and the presented pressure profiles are the strategies' predictions at the axial plane $x = 0.356$m (determined using the acoustic model).

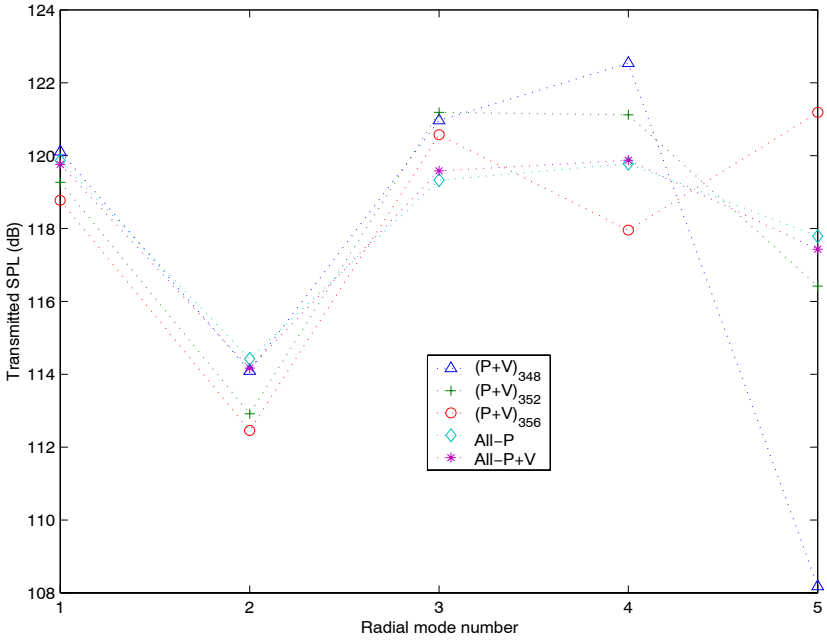

(a) SPL: Transmitted

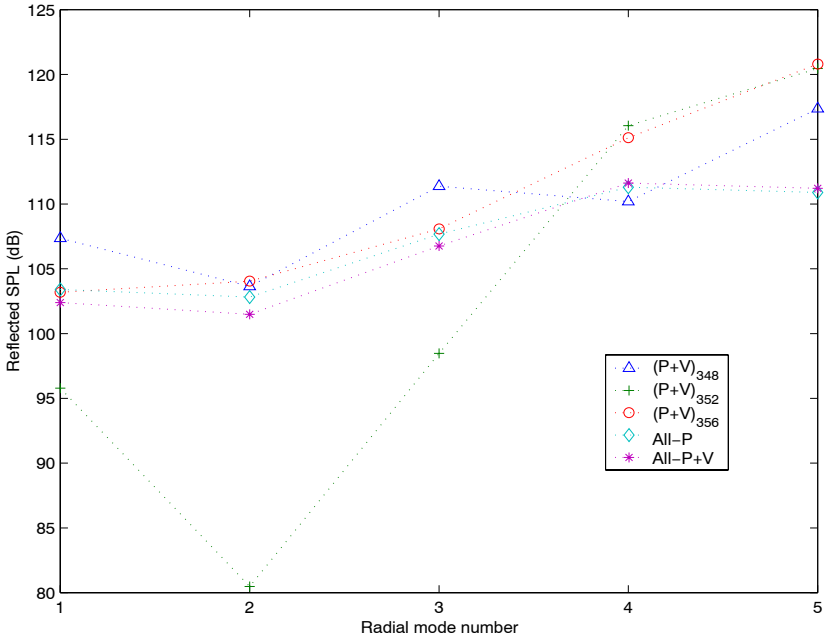

(b) SPL: Reflected

Figure 17: RR RESOUND bypass data: Modal SPL at the outer wall at $x = 0.356$m.

matching variable to describe the sound that we hear. If we then adopt this position of modelling and reproducing pressure perturbations as best we can, then the current set of data indicates strongly that an ideal method to use is the **All-P** triple-plane matching strategy. One gauge of its superior performance is demonstrated in the final two figures 16(a) and 16(b) that present pressure profiles from the matching strategies including reflections reconstructed at an axial plane **located at some distance downstream of the CFD/acoustic interface**. In this case the modal amplitudes were determined from CFD data at the three axial planes $x = 0.340$m, $x = 0.344$m and $x = 0.348$m, and these results, applied to our chosen acoustic model (uniform mean flow in a parallel duct), were subsequently used to predict the pressure profile further downstream at $x = 0.356$m. Only the **All-P** matching is able to represent closely the actual CFD profile given downstream and this, we believe, demonstrates a remarkable ability to extract acoustic information and behaviour from a complicated flow field.

For further comparison, transmitted and reflected modal SPL at the outer wall at a selected axial plane are presented in figure 17 for each matching strategy including reflections. The transmitted cut-on modal amplitudes appear to lie close to the 120dB mark, with the exception of the second radial mode, which is some 6dB lower. All matching strategies place the spurious reflections some $5\text{dB} - 15\text{dB}$ lower than their respective transmitted cut-on modes, with the fifth radial mode (closest to resonance) having the most significant reflected component.

4.7 RESOUND Fan/OGV test case in the bypass duct (DLR)

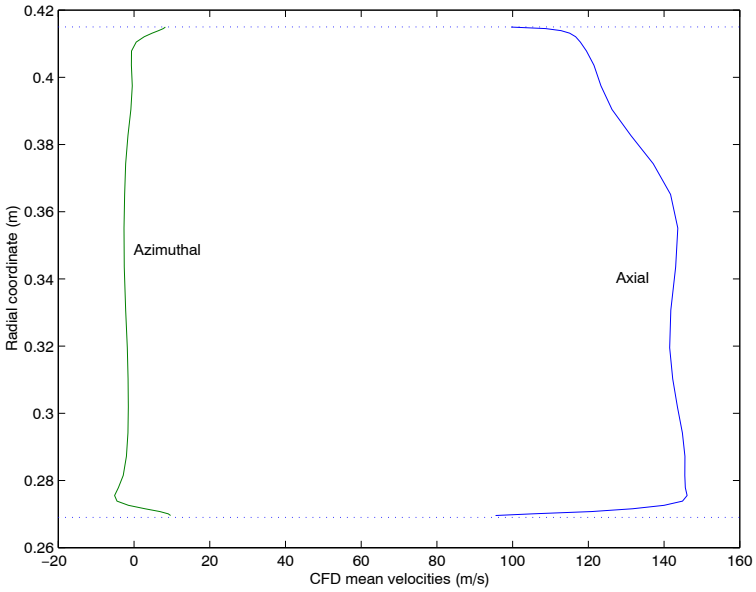

Figure 18: DLR data: Fan/OGV RESOUND testcase. Axial and azimuthal mean flow profiles from the CFD data at $x = 0.320$m.

Description of data

As well as Rolls-Royce, DLR also supplied flow-field data for the RESOUND Fan/OGV test case, which enabled our matching strategies to be tested a second time at the bypass interface (psogvex in figure 12).

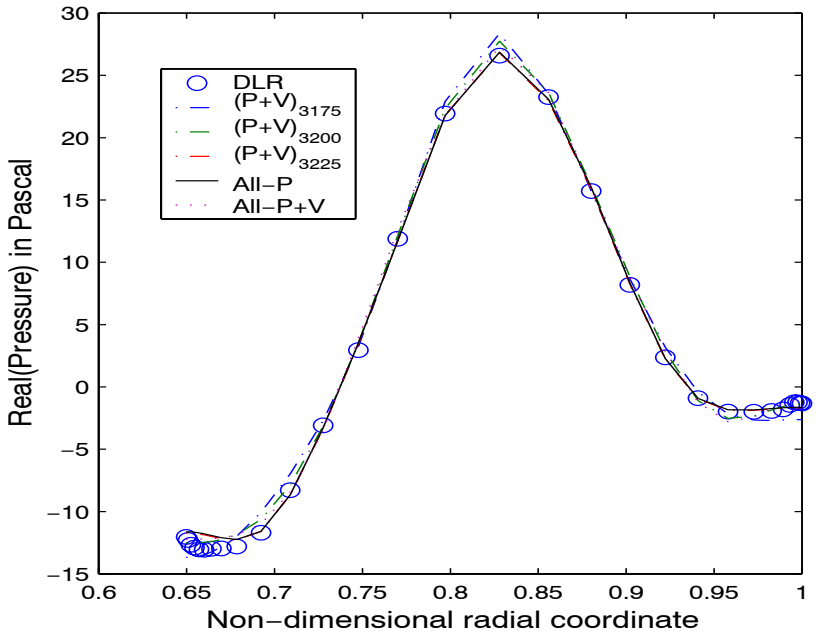

(a) Real Part: Unsteady Pressure Component

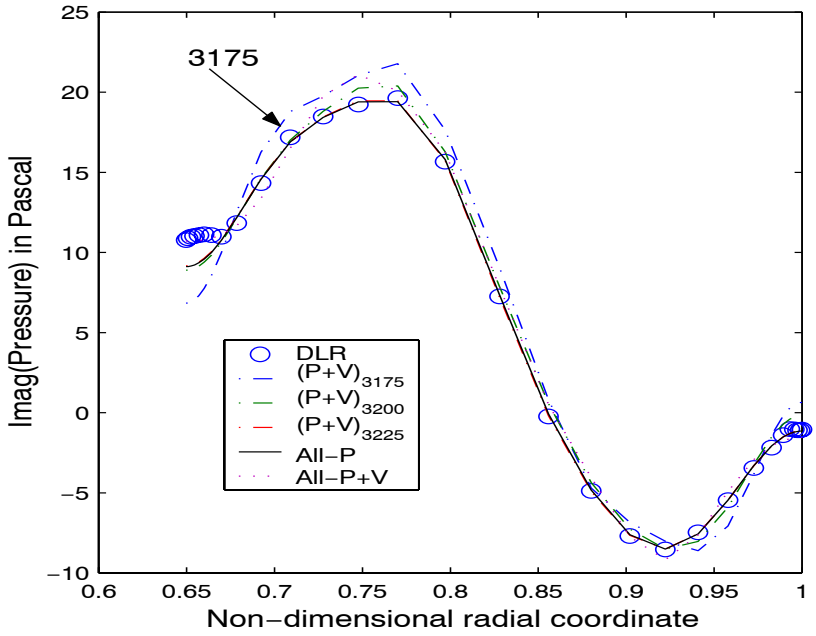

(b) Imag Part: Unsteady Pressure Component

Figure 19: DLR RESOUND bypass data: reconstructed unsteady pressure profiles at one of the *matched* axial planes, $x = 0.3225$m, for matching strategies that include reflections.

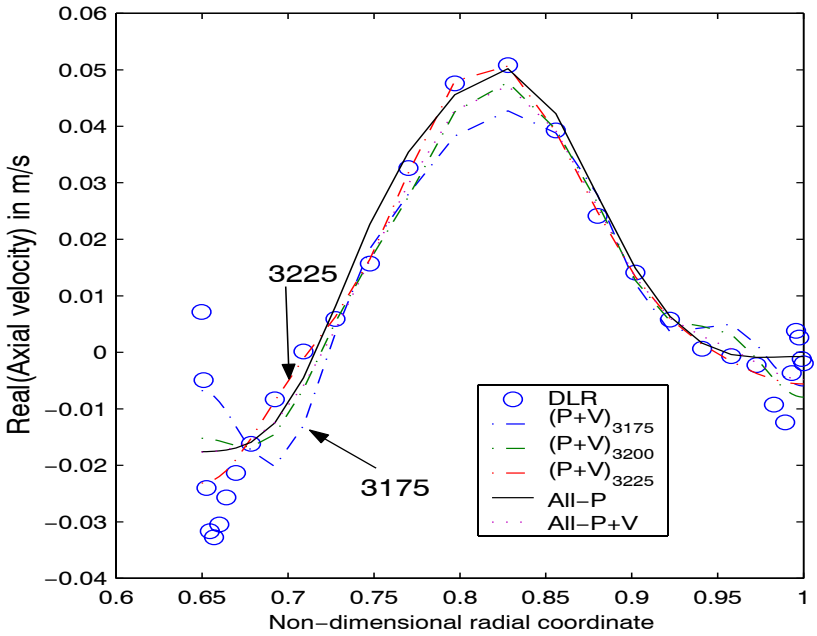

(a) Real Part: Unsteady Axial Velocity Component

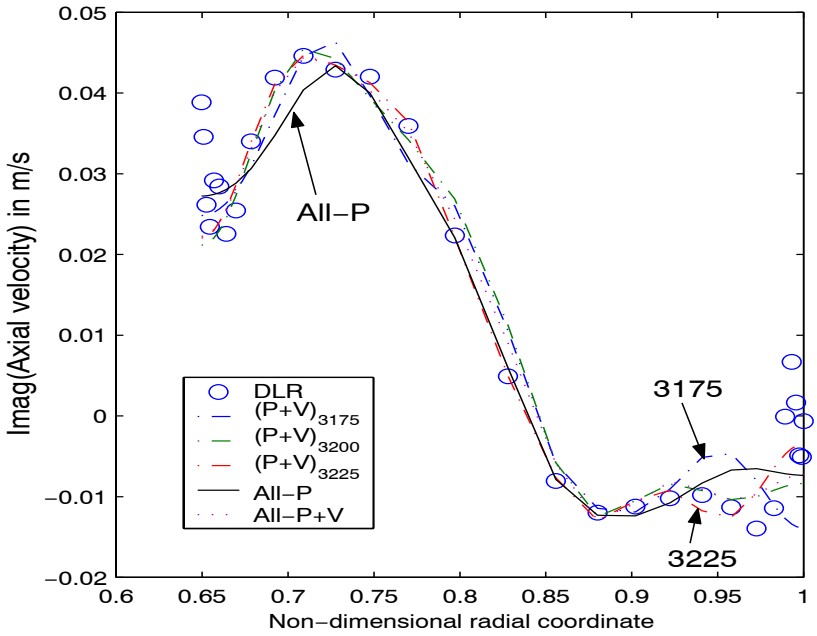

(b) Imag Part: Unsteady Axial Velocity Component

Figure 20: DLR RESOUND bypass data: reconstructed unsteady axial velocity profiles at one of the *matched* axial planes, $x = 0.3225$m, for matching strategies that include reflections.

Data was given at three axial planes equally spaced between $x = 0.3175$m and $x = 0.3225$m; these axial planes are not only closer to the OGVs than those supplied by Rolls-Royce, but the spacing between them is much smaller. Perturbation data was provided for a number of frequencies, but the most interesting set is the same frequency harmonic (2BPF) and circumferential wavenumber that was taken from Rolls-Royce. For the DLR case the Helmholtz number, based on the outer duct radius, is calculated to be 39.96 and the circumferential mode number is $m = +13$, implying that DLR's sense of azimuthal coordinate is clearly opposite to that of Rolls-Royce. The mean flow, as expected in the bypass duct, contains a significant vortical component and compares well to the Rolls-Royce mean flow shown in section 4.6. The mean flow is stripped as before to obtain a simple uniform flow with mean axial Mach number of $M = 0.40$. The hub-to-tip ratio across the axial planes is 0.649 to three decimal places and five cut-on modes are expected.

Results

The correct sign convention for the time decomposition was determined by comparing the axial time-averaged acoustic energy fluxes of the raw CFD data and the modal solution from the **All-P** strategy. The sign convention with the most realistic acoustic energy flux for the **All-P** matching and the lowest least-squares error residue was selected.

Perhaps the most striking feature of these results is how well all the strategies that include reflections mimic the CFD pressure and axial velocity perturbation data. The reconstructed profiles derived from each matching strategy that includes reflections for pressure and axial velocity perturbations can be seen in figures 19 and 20. Only one conclusion can be drawn from this: the unsteady velocity perturbation is almost completely irrotational with negligible vortical component. This contrasts strongly with the Rolls-Royce data of section 4.6, where the unsteady axial velocity profiles appear to possess a very large vortical component. The only vorticity that can be observed in the unsteady velocity profiles in this case appears close to the walls and well inside the boundary layers. Considering that the mean flow contains significant vorticity from the wakes of the fan and stators, it seems indeed surprising that no vorticity is present in the unsteady velocity perturbation.

Reflections are present in the flow field but their amplitudes are fairly low, approximately $7\% - 12\%$ of their respective incident cut-on modes. Figures 21(a) and 21(b) show the sound pressure levels on the outer wall of the middle interface ($x = 0.3200$m) for the transmitted and reflected components of the five cut-on radial modes. The transmitted modal amplitudes appear to lie roughly in the neighbourhood of 110dB with the respective reflected modal amplitudes around 90dB. The reflected amplitude of the first radial mode is clearly lower than those of the other cut-on modes. The **All-P** strategy possesses the highest reflections in general, but this may be more an indication of the type of non-reflecting boundary condition used by DLR than a problem of the actual matching strategy.

Table 4 contains the axial time-averaged acoustic energy flux of the raw CFD data and the derived modal solutions (from each matching strategy). Due to the irrotational nature of the velocity perturbation, the figures are in much closer agreement than for the Rolls-Royce RESOUND case. The slightly higher axial energy flux for the raw CFD data may well be attributed to the mean flow vorticity, but this is speculative.

5 Multi-plane slowly varying matching strategies

The results presented in previous sections indicate some distinct advantages of using a multi-plane strategy for matching between CFD and acoustic models. However, one obvious drawback with the **All-P**

Table 4: DLR RESOUND data: time-averaged acoustic energy flux (axial)

Raw CFD data	
X	Value
0.3175	0.2360 E-7
0.3200	0.2309 E-7
0.3225	0.2225 E-7

Strategies that include reflections				
$(P+V)_{3175}$	$(P+V)_{3200}$	$(P+V)_{3225}$	All P	All $P+V$
0.2134 E -7	0.2146 E-7	0.2140 E-7	0.2120 E-7	0.2132 E-7

Strategies assuming no reflections							
P_{3175}	P_{3200}	P_{3225}	PV_{3175}	PV_{3200}	PV_{3225}	$3P$	$3P+3V$
0.2254E-7	0.2018E-7	0.1780E-7	0.2177E-7	0.2102E-7	0.1973E-7	0.1994E-7	0.2076E-7

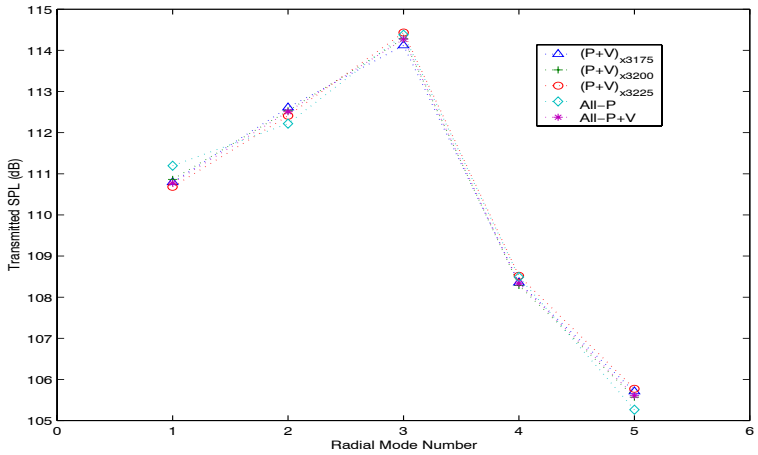

(a) SPL: Transmitted

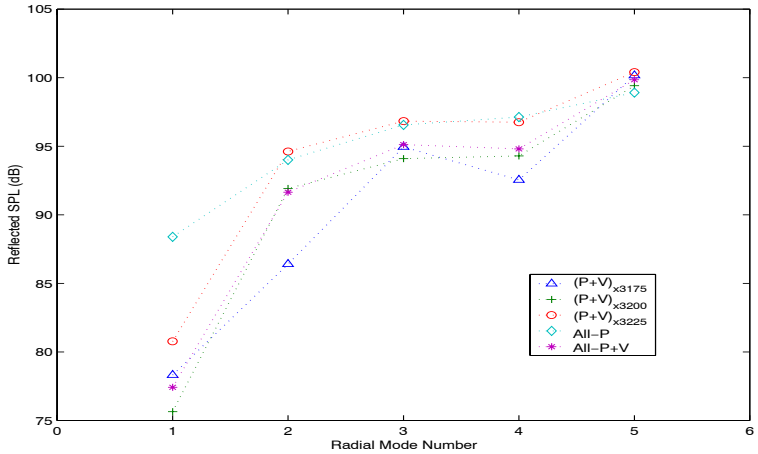

(b) SPL: Reflected

Figure 21: DLR RESOUND bypass data: Modal SPL at the outer wall at $x = 0.3200$m.

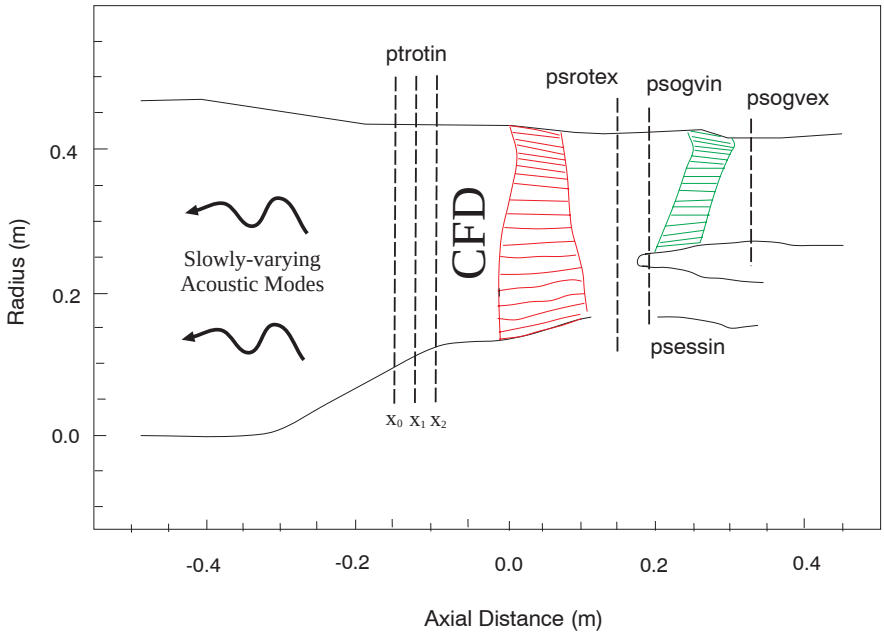

Figure 22: Fan/OGV RESOUND testcase geometry. Matching slowly-varying modes using CFD information at three axial planes at the inlet (ptrotin). The duct has hard walls.

and **All-P+V** strategies is that they require the three axial planes to lie in a section of the duct that is locally parallel. Taking the example of data from the RESOUND geometry supplied by Rolls-Royce and DLR (see sections 4.6 and 4.7), finding a locally parallel duct section is not a problem at the bypass-duct interface (psogvex) but, unless the interface is placed very near the fan, finding such a locally parallel duct section is very difficult at the inlet (ptrotin). In the case of a slowly converging or diverging region of a duct, the acoustic field can still be decomposed into **slowly varying modes**, as defined in [9, 15, 16]. If the CFD source field is to be matched onto an acoustic model that uses slowly varying modes, it makes sense to attempt a matching by decomposing the acoustic field into these modes. Based on the irrotational mean flow model of Rienstra [16], the multi-plane pressure-only matching strategy (**All-P**) is extended to derive modal amplitudes in a slowly varying duct. It may be useful to remark here that, in the limit of a duct becoming locally parallel, the slowly-varying modes tend to the usual infinite straight duct modes in any case.

We begin with CFD supplied mean flow and unsteady pressure data, which is Fourier decomposed in both time and azimuthal direction, at three axial planes $x_0 < x_1 < x_2$, such as in the case of an inlet matching for the RESOUND geometry in figure 22. The duct geometry is specified by two radial functions for the inner and outer walls, $R_1(x)$ and $R_2(x)$, respectively. As in the straight-duct matching, the flow field is non-dimensionalised by scaling all lengths by a typical duct radius R_∞, the density $\tilde{\rho}$ on some reference value ρ_∞, velocities $\tilde{\boldsymbol{v}}$ and sound speed $\tilde{c}$ on a reference sound speed c_∞, time $\tilde{t}$ on R_∞/c_∞ and pressure $\tilde{p}$ on $\rho_\infty c_\infty^2$. For the acoustic model, the flow field can be expressed as a mean flow plus harmonic perturbations of a given non-dimensional angular frequency ω and circumferential wavenumber m,

$$\left[\tilde{\boldsymbol{v}},\, \tilde{\rho},\, \tilde{p},\, \tilde{c}\right] = [\boldsymbol{V},\, D,\, P,\, C] + [\nabla\phi_{\omega m},\, \rho_{\omega m},\, p_{\omega m},\, c_{\omega m}]e^{\mathrm{i}\omega t - \mathrm{i}m\theta}$$

Assuming here that this model is based around an irrotational mean flow, such as in [16], the mean axial velocity, the mean density, the mean sound speed and the mean pressure must be function of a **slow axial variable** $X = \epsilon x$**,** $\epsilon \ll 1$ **only**. This small parameter ϵ is representative of the typical non-dimensional axial variation of the duct (and therefore should be small) and can be ignored in the practical matching application, being only necessary here to legitimise the multiple-scales method. Thus,

$$\boldsymbol{V}(X, r; \epsilon) = U(X)\boldsymbol{e}_x + \epsilon V(X, r)\boldsymbol{e}_r + O(\epsilon^2), \tag{36a}$$

$$D(X, r; \epsilon) = D(X) + O(\epsilon^2), \tag{36b}$$

$$C(X, r; \epsilon) = C(X) + O(\epsilon^2), \tag{36c}$$

$$P(X, r; \epsilon) = P(X) + O(\epsilon^2), \tag{36d}$$

where $\boldsymbol{e}_x$ and $\boldsymbol{e}_r$ are unit vectors in the axial and radial directions respectively. The mean flow field satisfies the equations

$$U(X) = \frac{F}{D(X)\left(R_2^2(X) - R_1^2(X)\right)} \quad \text{and} \quad \frac{1}{2}\left(\frac{F}{D(R_2^2 - R_1^2)}\right)^2 + \frac{1}{\gamma - 1}D^{\gamma-1} = E, \tag{37}$$

where γ is the constant ratio of specific heats at constant pressure and volume, $P = \frac{1}{\gamma}D^{\gamma}$ and $C = D^{(\gamma-1)/2}$. The two parameters F and E determine the entire mean flow field and must be chosen to fit the CFD mean flow data as ideally as possible. The mean flow from the CFD must therefore be stripped of any swirling and vortical component to make the velocity nearly uniform axially. Given that πF is the mass flux through an axial plane, F can be found by determining the average mass flux of the mean flow at the three axial planes given. The other parameter E can be obtained by a similar averaging process of the mean density or, indeed, the mean pressure or mean sound speed if they are regarded as more suitable.

Once a mean flow consistent with the acoustic model and *representative* of the steady part of the CFD data has been derived, the Fourier-decomposed (ω, m) component of the pressure can be written in the following way

$$p_{\omega m}(X, r) = \sum_{\mu=1}^{M} A_{m\mu}\psi_{m\mu}(X, r) + \sum_{\mu=-M}^{-1} A_{m\mu}\psi_{m\mu}(X, r). \tag{38}$$

The functions $\psi_{m\mu}$ represent the basis functions for the right-running ($\mu > 0$) and left-running ($\mu < 0$) slowly varying pressure modes, which take the form [16]

$$\psi_{m\mu} = -\mathrm{i}D(X)(\omega - \kappa_{m\mu}(X)U(X))\left[N_{m\mu}(X)\,\mathrm{J}_m(\alpha_{m\mu}(X)r) + M_{m\mu}(X)\,\mathrm{Y}_m(\alpha_{m\mu}(X)r)\right]e^{-\mathrm{i}\int_{X_s}^{X}\kappa_{m\mu}(\xi)\mathrm{d}\xi}. \tag{39}$$

Here, X_s is the axial position chosen to become the virtual source plane of the acoustic model and J_m and Y_m are m-th order Bessel functions of the first and second kind respectively [17]. The slowly-varying radial eigenvalues $\alpha_{m\mu}$ are found from the hard-wall boundary condition and the axial eigenvalues $\kappa_{m\mu}$ can be subsequently derived for each $\alpha_{m\mu}$ via a slowly varying dispersion relation. The functions $N_{m\mu}$ and $M_{m\mu}$, which are determined by a solvability condition, dictate how the modal amplitude changes axially through the duct. They can be suitably normalized to give, for instance, a modal contribution of $A_{m\mu}$ to either the unsteady pressure $p_{\omega m}$ or unsteady velocity potential $\phi_{\omega m}$ at the outer wall at position $X = X_s$.

Hence, given the Fourier-decomposed CFD pressure data $\mathcal{P}_{\omega mi}(r)$ at each $X = X_i$, we can write

$$\mathcal{P}_{\omega mi}(r) = \sum_{\mu=1}^{M} A_{m\mu}\psi_{m\mu}(X_i, r) + \sum_{\mu=-M}^{-1} A_{m\mu}\psi_{m\mu}(X_i, r). \tag{40}$$

Subsequently, we can define three sets of radial basis functions $\psi_{m\mu}(X_i, r)$ for $i = 0$, 1 and 2 in a similar manner as those defined in the multi-plane **All-P** matching strategy. The most important difference here is that the three sets of basis function are valid on three different radial intervals, $R_1(X_i) \leq r \leq R_2(X_i)$ for $i = 0$, 1 and 2 respectively.

In describing the locally-parallel multi-plane method (see section 3.4), it was argued that a subtle rescaling of the unknown modal amplitudes is required, prior to minimising the least-squares error, to carefully balance the exponential behaviour of left- and right-running strongly cut-off modes across the three axial planes. The same treatment is also necessary here and the *rescaled* modal amplitudes $A^+_{m\mu}$ and $A^-_{m\mu}$, for left- and right-running modes respectively, are defined as

$$A_{m\mu} = \begin{cases} A^+_{m\mu} e^{-\mathrm{i}\int_{X_0}^{X_s} \kappa_{m\mu}(\xi)\,\mathrm{d}\xi} & \text{for } \mu > 0, \\ A^-_{m\mu} e^{-\mathrm{i}\int_{X_2}^{X_s} \kappa_{m\mu}(\xi)\,\mathrm{d}\xi} & \text{for } \mu < 0. \end{cases} \tag{41}$$

Substitution of these rescaled amplitudes into (40) gives

$$\mathcal{P}_{\omega mi}(r) = \sum_{\mu=1}^{M} A^+_{m\mu}\zeta_{m\mu}(X_i, r) + \sum_{\mu=-M}^{-1} A^-_{m\mu}\zeta_{m\mu}(X_i, r), \tag{42}$$

where

$$\zeta_{m\mu}(X_i, r) = \begin{cases} \psi_{m\mu}(X_i, r) e^{-\mathrm{i}\int_{X_0}^{X_i} \kappa_{m\mu}(\xi)\,\mathrm{d}\xi} & \text{for } \mu > 0, \\ \psi_{m\mu}(X_i, r) e^{-\mathrm{i}\int_{X_2}^{X_i} \kappa_{m\mu}(\xi)\,\mathrm{d}\xi} & \text{for } \mu < 0. \end{cases}$$

To perform the least-squares minimisation, we multiply (42) by the respective conjugate basis functions $\zeta^*_{m\nu}(X_i, r)$ for $\nu = -M, \ldots, -1, 1, \ldots, M$ and integrate across the duct at each axial plane $X = X_i$ to obtain the three matrix equations

$$\mathcal{M}_i \boldsymbol{a} = \boldsymbol{p}_i$$

where

$$\{\mathcal{M}_i\}_{\mu\nu} = \int_{R_1(x_i)}^{R_2(x_i)} \zeta_{m\mu}(x_i, r)\zeta^*_{m\nu}(x_i, r) r\,\mathrm{d}r, \quad \{\boldsymbol{a}\}_\mu = \begin{cases} A^+_{m\mu} & \text{for } \mu > 0, \\ A^-_{m\mu} & \text{for } \mu < 0, \end{cases}$$

$$\{\boldsymbol{p}_i\}_\nu = \int_{R_1(x_i)}^{R_2(x_i)} \mathcal{P}_{\omega mi}(r)\zeta^*_{m\nu}(x_i, r) r\,\mathrm{d}r.$$

As in the locally parallel duct case, the least-squares approach subsequently finds the set of modal amplitudes $\boldsymbol{a}$ that minimises the cost function

$$\sum_{i=0}^{2} \left\| \mathcal{M}_i \boldsymbol{a} - \boldsymbol{p}_i \right\|^2.$$

Finally, the actual modal amplitudes $A_{m\mu}$ at $X = X_s$ can be recovered from $\boldsymbol{a}$ by inverting the applied scaling defined in (41).

Using the above method, it is now possible to extend the multi-plane method to converging and diverging ducts. A further extension to enable matching in duct section with finite impedance walls is also possible, by adopting the slowly varying basis functions derived from Myers's finite-impedance boundary condition [18]. Whilst the effects of the non-orthogonality of impedance wall modes remains an issue to be assessed, it is possible to demonstrate that the current method works in principle using soft-wall

modes. Figure 23 shows three pressure profiles taken from the Rolls-Royce RESOUND test data (with hard walls) and a modal reconstruction using (a) ten hard-wall modes and (b) 10 soft-wall modes, where the outer wall non-dimensional impedance has been taken to be $Z = 2 + \mathrm{i}$. Notice that the least-squares method can still achieve a very good fit in core of the duct, but not so near the outer wall where the soft-wall modal behaviour differs greatly from that of hard-wall modes. More testing of the matching strategy in both hard-walled and soft-walled ducts is needed.

The slowly-varying multi-plane strategy, in principle, can be applied at any axial position within a duct with axisymmetric geometry, although its validity will depend on how close the CFD mean flow is to the form assumed for the acoustic model. Crucially, it is also important to avoid matching across or near a region where transition [19] or near-transition [20] could occur, due to the presence of a full or partial reflection of a radial mode. This may, in turn, generate a large residual error in the least-squares minimisation and misleading results.

6 Conclusions

Whilst not enough analysis has been carried out to draw concrete conclusions concerning the development of an optimal strategy, the investigations performed on our four real CFD data sets yielded some very important and even surprising observations. These observations have enabled us to at least suggest the form an optimal matching strategy might take. Out of the cases examined, we have been rather fortunate, because it has been possible to clearly observe the effects of both spurious reflections at boundaries (section 4.5) and vorticity contamination of the velocity field (the exhaust matching in section 4.3) in isolation from each other.

Lacking a clear understanding of *acoustic energy*, we must rely on reproducing the pressure field as accurately as possible in order to represent the sound that we hear. The pressure field is only balanced by the solenoidal part of the velocity field and, in a uniform mean flow, this remains entirely decoupled from the vortical part. Our results indicate that the acoustic pressure perturbations are best matched using a triple-plane matching strategy (TPMS) that applies a least-square minimisation of the error in the pressure profiles at three neighbouring axial planes and determines both transmitted and reflected modes. The **All-P** triple-plane matching strategy displays a remarkable ability to extract acoustic information from the complex flow field in the bypass duct of the RESOUND geometry (section 4.6). We conclude that this procedure is especially ideal in areas of the duct where the velocity field contains a strong vortical component (such as the bypass duct) making velocity data unsuitable for matching.

One other benefit of a multi-plane strategy is the amount of useful information and cross-checking it provides. By calculating the Myers's time-averaged acoustic energy flux axially for the **All-P** triple-plane matching strategy and comparing it to the flux of the raw CFD data, it is possible to check whether the acoustic model adopts the **same sign convention** in the Fourier time decomposition as used by the CFD partner in post-processing. However, there is no way of telling which sign convention has been taken in the circumferential decomposition and extra care must be taken at the CFD-level to ensure that the correct circumferential mode is examined; this is because the sense of rotation is very important in many circumstances (where there are interactions with stator vanes or mean swirl for instance).

Of course, it should be realised that our conclusions can only be applied to the simple acoustic model where uniform mean flow and hard walls are assumed. More work is obviously needed to optimise the matching of CFD and acoustic models at an in-duct interface. This includes more tests of real data to further confirm our initial results, in particular the success of the **All-P** triple-plane matching

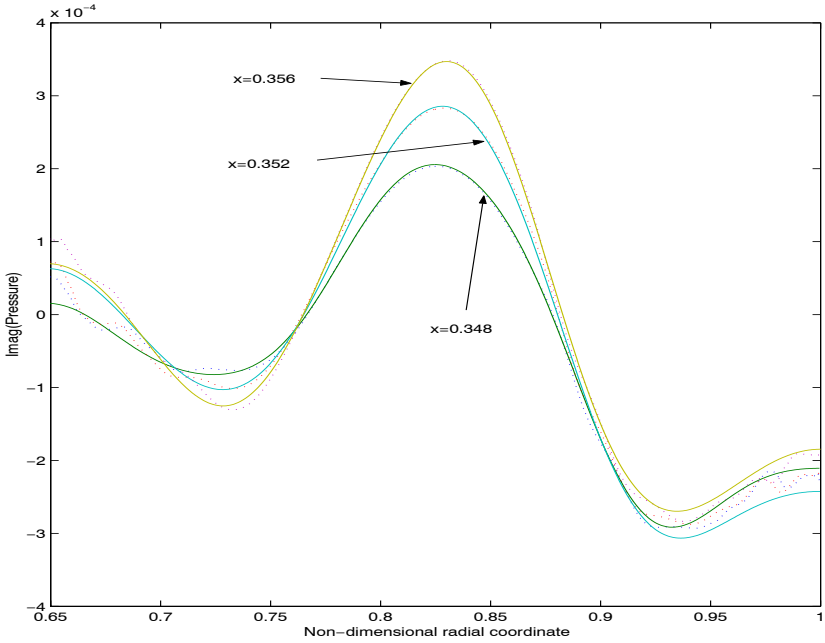

(a) Hard Wall Modes.

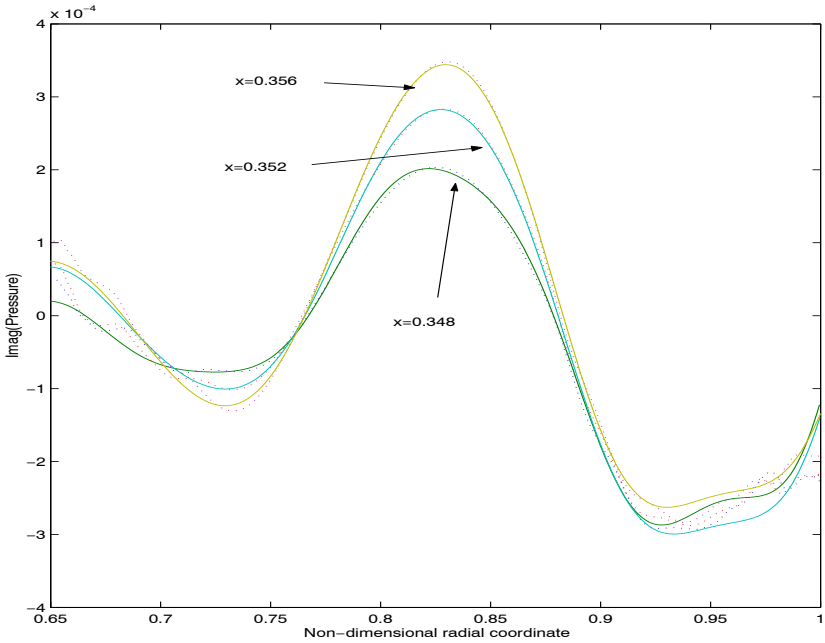

(b) Soft Wall Modes.

Figure 23: Examination of applying the triple-plane pressure matching using soft-wall modes. Here, unsteady pressure data from the RR RESOUND testcase (section 4.6) at three neighbouring axial planes is matched assuming that either (a) both inner and outer walls are hard or (b) the inner wall is hard, but the outer wall has a non-dimensional impedance of $Z = 2 + \mathrm{i}$. The first ten radial modes are taken in each case. The dotted lines are the original unsteady pressure profiles from the CFD data, while the solid lines are derived at each axial plane from the modal solution.

strategy. In section 5 we have demonstrated that the multi-plane pressure-only strategy can be applied to **converging and diverging ducts** and with both **hard and impedance walls**. This must be regarded as quite an important step forward in the development of a robust matching strategy, although more testing is required to fully validate the method. Of particular concern is the effect of the non-orthogonality of soft-wall modes. There is, of course, other opportunities to extend the strategy further to cases with mean vortical or swirling flow although there will be some difficulties including (a) strong interactions with the vortical component of the flow-field and (b) how to treat the continuous part of the modal spectrum. Even work on more minor issues, such as improving the directional resolution of modes near resonance, is needed.

Beyond just the formulation of a matching strategy, the analysis in this document reveals the necessity for a greater understanding of acoustic energy in non-uniform flow. The falling value of the time-averaged acoustic energy flux (Myers's definition) away from the source, which was observed in the RESOUND bypass duct with parallel mean flow in section 4.6, warrants more serious investigation, particularly in isolating the mechanisms of acoustical-vortical interaction .

7 Acknowledgements

This work was carried out under the project "TurboNoise CFD" of the European Union's Fifth Framework Programme. We would like to thank all the CFD partners involved for their assistance in providing real data to test the proposed matching strategies.

8 A proposed matching procedure

Here, we describe a procedure for matching CFD data to an acoustic model assuming a parallel or slowly varying cylindrical duct with irrotational (quasi-uniform) mean flow:

1. Consider the geometry. Three neighbouring axial planes should be chosen in a part of the duct to act as an interface. The duct walls can either be hard or of finite impedance. The mean flow should be (approximately) axisymmetric without a significant swirling component. Try to avoid locations where reflection or partial reflection of a radial mode may occur.

2. The total flow field, produced by the CFD calculations at the interface, has to be split into a steady part (the mean flow) and an unsteady part for each multiple $\omega = n\Omega$ of the first harmonic Ω and circumferential m-mode considered (the perturbations). A logical approach is via Fourier transformations in t and θ, after which all frequencies and m-modes of interest are available. If the mean flow is not axisymmetric (*i.e.* θ-dependent), the $(m = 0)$ component is automatically the flow field's average over θ.

   So, for a physical quantity $f(x, r, \theta, t)$, given at the three axial planes $x_i(r) = \tilde{x}_i + \lambda(r)$, we derive the mean flow quantity $F_i(r)$ and the unsteady (m, ω)-Fourier component $\mathcal{F}_{im}(r; \omega)$ as follows. If f is periodic in time with period $2\pi/\Omega$ (radial frequency Ω), it can be written as

$$f(x_i, r, \theta, t) = \sum_{n=-\infty}^{\infty} \sum_{m=-\infty}^{\infty} \hat{f}_m(r; n\Omega)\, \mathrm{e}^{\mathrm{i}n\Omega t - \mathrm{i}m\theta} \,. \tag{43}$$

Each Fourier component is given by

$$\hat{f}_m(r; n\Omega) = \frac{\Omega}{4\pi^2} \int_0^{2\pi} \int_0^{2\pi/\Omega} f(x_i, r, \theta, t)\, \mathrm{e}^{\mathrm{i}m\theta - \mathrm{i}n\Omega t}\, \mathrm{d}t\, \mathrm{d}\theta, \tag{44}$$

where one should note the $\pm\mathrm{i}$ and 2π conventions. We have then (*c.f.* equation 72, 91)

$$F_i(r) = \hat{f}_0(r; 0) \tag{45a}$$

$$\mathcal{F}_{\omega m i}(r; \omega) = \hat{f}_m(r; \omega). \tag{45b}$$

If the CFD results refer to a single rotor stage, they are effectively steady in a co-rotating frame of reference. If, in addition, the field is periodic in θ with period $2\pi/B$ (B blades, say), the above Fourier transformation may be simplified as follows. We write our field function as

$$f(x_i, r, \theta, t) = g(x_i, r, \theta - \Omega t) = \sum_{n=-\infty}^{\infty} \sum_{m=-\infty}^{\infty} \hat{g}_m(r; n\Omega)\, \mathrm{e}^{\mathrm{i}n\Omega t - \mathrm{i}mB\theta} \tag{46}$$

Now the double Fourier integrals reduce to a single one, while most of the Fourier coefficients $\hat{g}_m(r; n\Omega)$ vanish:

$$\hat{g}_m(r; n\Omega) = \frac{1}{2\pi} \delta_{n,mB} \int_0^{2\pi} g\big(x_i, r, \tfrac{\xi}{B}\big)\, \mathrm{e}^{\mathrm{i}\xi}\, \mathrm{d}\xi\,. \tag{47}$$

3. The mean flow variables from the CFD data will almost certainly not form a consistent solution of the mean flow equations which correspond to the acoustic model considered. Depending on the model, the mean flow must be **stripped** by removing any swirl component and averaging out any radial variations of axial velocity, density, temperature and sound speed; mass flux should be conserved if possible. For this reason, one must be careful to judge just how reasonable the acoustic model's assumptions are in respect to the CFD data supplied.

4. Once the uniform mean flow is known, the acoustic modal equations can be solved for the circumferential mode numbers m of interest and the matrices $\mathcal{M}_i$ and vectors $\boldsymbol{p}_i$ etc. of the matrix equations can be formed using the available basis functions.

5. In the case of a locally parallel duct, the mode matching is performed by a pressure-only triple-plane matching strategy, described as **All-P** in section 4. The method includes resolving any spurious reflections. In certain circumstances where the velocity is known to be irrotational, the triple-plane matching strategy employing both pressure and axial velocity (**All-P+V** in section 4) can also be used. For a locally converging or diverging duct, the slowly varying multi-plane strategy from section 5 must be used.

6. To check that the same sign convention for Fourier decomposition in time has been adopted by both the CFD post-processing in Step 2 and the acoustic model, the axial time-averaged acoustic energy flux of the CFD data should be compared to the value derived from the either the **All-P** or slowly varying multi-plane method. The least-squares errors from the two sign conventions should also be compared.

7. The least-squares error will provide a good measure of the model-jump. Any spurious reflections are partly caused by the model jump, but by careful assessment of the reflected amplitudes, in conjunction with the least-squares error, the performance of any non-reflecting boundary conditions can be measured and even improved.

Appendix
Acoustic models and modal solutions.

A Summary of equations for fluid motion

For future reference we will describe here a large number of possible acoustic models, systematically derived from the compressible Navier-Stokes equations, under the assumptions of absence of friction, absence of thermal conduction and the fluid being a perfect gas. The flow is described by a steady mean flow and small perturbations, upon which linearization and Fourier time-analysis is possible. Further simplifications are considered based on axisymmetrical geometry and mean flow.

A.1 Conservation laws and constitutive equations

The original laws of mass, momentum and energy conservation, written in terms of pressure p, density ρ, velocity vector $\boldsymbol{v}$, scalar velocity $v = |\boldsymbol{v}|$, viscous stress tensor $\boldsymbol{\tau}$, internal energy density ϵ, total energy density e and heat flux vector $\boldsymbol{q}$, are given by

$$\text{mass:} \quad \tfrac{\partial}{\partial t}\rho \quad + \nabla\cdot(\rho\boldsymbol{v}) \quad = 0 \tag{48a}$$

$$\text{mom.:} \quad \tfrac{\partial}{\partial t}(\rho\boldsymbol{v}) + \nabla\cdot(\rho\boldsymbol{v}\boldsymbol{v}) = -\nabla p + \nabla\cdot\boldsymbol{\tau} \tag{48b}$$

$$\text{energy:} \quad \tfrac{\partial}{\partial t}(\rho e) + \nabla\cdot(\rho e\boldsymbol{v}) = -\nabla\cdot\boldsymbol{q} - \nabla\cdot(p\boldsymbol{v}) + \nabla\cdot(\boldsymbol{\tau}\boldsymbol{v}) \tag{48c}$$

while

$$e = \epsilon + \tfrac{1}{2}v^2. \tag{48d}$$

Depending of the application, it is often convenient to introduce the enthalpy or heat function

$$h = \epsilon + \frac{p}{\rho}, \tag{49}$$

and/or entropy s and temperature T via the fundamental law of thermodynamics for a reversible process

$$T\mathrm{d}s = \mathrm{d}\epsilon + p\mathrm{d}\rho^{-1} = \mathrm{d}h - \rho^{-1}\mathrm{d}p. \tag{50}$$

With $\frac{\mathrm{d}}{\mathrm{d}t} = \frac{\partial}{\partial t} + \boldsymbol{v}\cdot\nabla$ for the convective derivative, the above conservation laws may be reduced to

$$\text{mass:} \quad \tfrac{\mathrm{d}}{\mathrm{d}t}\rho = -\rho\nabla\cdot\boldsymbol{v} \tag{51a}$$

$$\text{momentum:} \quad \rho\tfrac{\mathrm{d}}{\mathrm{d}t}\boldsymbol{v} = -\nabla p + \nabla\cdot\boldsymbol{\tau} \tag{51b}$$

$$\text{energy :} \quad \rho\tfrac{\mathrm{d}}{\mathrm{d}t}\epsilon = -\nabla\cdot\boldsymbol{q} - p\nabla\cdot\boldsymbol{v} + \boldsymbol{\tau}:\nabla\boldsymbol{v} \tag{51c}$$

$$\rho\tfrac{\mathrm{d}}{\mathrm{d}t}h = \tfrac{\mathrm{d}}{\mathrm{d}t}p - \nabla\cdot\boldsymbol{q} + \boldsymbol{\tau}:\nabla\boldsymbol{v} \tag{51d}$$

$$\rho T\tfrac{\mathrm{d}}{\mathrm{d}t}s = -\nabla\cdot\boldsymbol{q} + \boldsymbol{\tau}:\nabla\boldsymbol{v}. \tag{51e}$$

For acoustic applications the entropy form (51e) is the most convenient to use.

For an *ideal* gas we have the following relations

$$p = \rho \mathcal{R} T, \tag{52a}$$
$$\mathrm{d}\epsilon = C_V \mathrm{d}T, \tag{52b}$$
$$\mathrm{d}h = C_P \mathrm{d}T, \tag{52c}$$

where C_V is the heat capacity or specific heat at constant volume, C_P is the heat capacity or specific heat at constant pressure [21] and both C_V and C_P may be functions of T. Both the specific gas constant $\mathcal{R}$ and the Poisson ratio γ can be taken to be practically constant and given by (the figures refer to air)

$$\mathcal{R} = C_P - C_V = 286.73 \text{ J/kg K}, \qquad \gamma = \frac{C_P}{C_V} = 1.402. \tag{53}$$

From equation (50) it then follows for an ideal gas that

$$\mathrm{d}s = C_V \frac{\mathrm{d}p}{p} - C_P \frac{\mathrm{d}\rho}{\rho} \tag{54}$$

while isentropic perturbations ($\mathrm{d}s = 0$), like sound, propagate with sound speed c given by the expression

$$c^2 = \left(\frac{\partial p}{\partial \rho}\right)_s = \frac{\gamma p}{\rho} = \gamma \mathcal{R} T. \tag{55}$$

In the case of a *perfect* gas, the specific heats are constant and we can integrate (apart from an immaterial integration constant) the equations (52) to obtain

$$\epsilon = C_V T, \tag{56a}$$
$$h = C_P T, \tag{56b}$$
$$s = C_V \log p - C_P \log \rho. \tag{56c}$$

A.2 In a rotating frame of reference

For axes rotating steadily relative to the absolute frame of reference, we have to include fictitious body forces due to rotation. If the moving frame of reference is rotating with angular velocity $\boldsymbol{\Omega}$ and $\boldsymbol{x}$ is the relative position vector, the absolute velocity is given by $\boldsymbol{v}_{\text{abs}} = \boldsymbol{v} + \boldsymbol{\Omega} \times \boldsymbol{x}$ and the equations (48) take the form

$$\text{mass:} \quad \tfrac{\partial}{\partial t}\rho \quad + \nabla \cdot (\rho \boldsymbol{v}) \quad = 0 \tag{57a}$$
$$\text{mom.:} \quad \tfrac{\partial}{\partial t}(\rho \boldsymbol{v}) + \nabla \cdot (\rho \boldsymbol{v}\boldsymbol{v}) = -2\boldsymbol{\Omega} \times \boldsymbol{v} - \boldsymbol{\Omega} \times (\boldsymbol{\Omega} \times \boldsymbol{x}) - \nabla p + \nabla \cdot \boldsymbol{\tau} \tag{57b}$$
$$\text{energy:} \quad \tfrac{\partial}{\partial t}(\rho e) + \nabla \cdot (\rho e \boldsymbol{v}) = -\nabla \cdot \boldsymbol{q} - \nabla \cdot (p \boldsymbol{v}) + \nabla \cdot (\boldsymbol{\tau} \boldsymbol{v}) \tag{57c}$$

where

$$e = \epsilon + \tfrac{1}{2}\left(v^2 + |\boldsymbol{\Omega}|^2 |\boldsymbol{x}|^2 - (\boldsymbol{\Omega} \cdot \boldsymbol{x})^2\right). \tag{57d}$$

If $\boldsymbol{\Omega} = \Omega \boldsymbol{e}_x$ and r is the radial coordinate in the cylindrical coordinate system (x, r, θ), this simplifies to

$$e = \epsilon + \tfrac{1}{2} v^2 + \tfrac{1}{2} \Omega^2 r^2. \tag{57e}$$

A.3 Acoustic applications

In the acoustic realm to be considered, the viscous or turbulent stress terms are assumed to play a role only within the source region, while any perturbation is assumed to be too fast to be affected by thermal conduction. Therefore, for present applications of acoustic propagation we intend to ignore viscous shear stress ($\boldsymbol{\tau}$) and thermal conduction ($\boldsymbol{q}$), so that we have

$$\tfrac{\mathrm{d}}{\mathrm{d}t}\rho = -\rho\nabla\cdot\boldsymbol{v}, \tag{58a}$$

$$\rho\tfrac{\mathrm{d}}{\mathrm{d}t}\boldsymbol{v} = -\nabla p, \tag{58b}$$

$$\tfrac{\mathrm{d}}{\mathrm{d}t}s = 0. \tag{58c}$$

This means that entropy remains constant and thus $\mathrm{d}h = \rho^{-1}\mathrm{d}p$ along pathlines.

Furthermore, we will assume the gas to be perfect, with the following thermodynamical closure relations

$$s = C_V \log p - C_P \log \rho, \quad c^2 = \frac{\gamma p}{\rho}. \tag{58d}$$

A.4 Perturbations of a mean flow

When we have a steady mean flow with unsteady perturbations, given by

$$\boldsymbol{v} = \boldsymbol{V} + \boldsymbol{v}', \quad p = P + p', \quad \rho = D + \rho', \quad s = S + s' \tag{59}$$

and linearize for small amplitudes, we subsequently obtain for the mean flow

$$\nabla\cdot\big(D\boldsymbol{V}\big) = 0, \tag{60a}$$

$$D\big(\boldsymbol{V}\cdot\nabla\big)\boldsymbol{V} = -\nabla P, \tag{60b}$$

$$\big(\boldsymbol{V}\cdot\nabla\big)S = 0, \tag{60c}$$

with

$$S = C_V \log P - C_P \log D, \quad C^2 = \frac{\gamma P}{D}. \tag{60d}$$

The perturbations are governed by

$$\tfrac{\partial}{\partial t}\rho' + \nabla\cdot\big(\boldsymbol{V}\rho' + \boldsymbol{v}'D\big) = 0 \tag{61a}$$

$$D\big(\tfrac{\partial}{\partial t} + \boldsymbol{V}\cdot\nabla\big)\boldsymbol{v}' + D\big(\boldsymbol{v}'\cdot\nabla\big)\boldsymbol{V} + \rho'\big(\boldsymbol{V}\cdot\nabla\big)\boldsymbol{V} = -\nabla p' \tag{61b}$$

$$\big(\tfrac{\partial}{\partial t} + \boldsymbol{V}\cdot\nabla\big)s' + \boldsymbol{v}'\cdot\nabla S = 0 \tag{61c}$$

with

$$s' = \frac{C_V}{P}p' - \frac{C_P}{D}\rho', \quad c' = \tfrac{1}{2}C\Big(\frac{p'}{P} - \frac{\rho'}{D}\Big). \tag{61d}$$

The expression for c' usually serves no purpose in linear acoustics.

A.5 Bernoulli for the mean flow

Since S remains constant along streamlines, we can introduce the mean flow enthalpy H, with $\mathrm{d}H = D^{-1}\mathrm{d}P$. On integrating the momentum equation (60b)

$$\boldsymbol{V}\cdot\nabla\boldsymbol{V} = \tfrac{1}{2}\nabla V^2 + (\nabla\times\boldsymbol{V})\times\boldsymbol{V} = -D^{-1}\nabla P = -\nabla H \tag{62}$$

along a streamline, noting that $(\nabla\times\boldsymbol{V})\times\boldsymbol{V}$ is orthogonal to $\boldsymbol{V}$ and therefore to the streamline, we obtain for the mean flow a form of Bernoulli's equation as follows:

$$\tfrac{1}{2}V^2 + H = \text{constant along a streamline.} \tag{63}$$

A.6 Homentropic mean flow

If the mean flow is homentropic ($S =$ constant), for example when P and D are constant, the perturbations are isentropic along streamlines and the pressure and density are related by

$$\big(\tfrac{\partial}{\partial t} + \boldsymbol{V}\cdot\nabla\big)p' = C^2\big(\tfrac{\partial}{\partial t} + \boldsymbol{V}\cdot\nabla\big)\rho' \tag{64}$$

A.7 Isentropic perturbations

If the perturbations are entirely isentropic ($s' \equiv 0$), for example when $\boldsymbol{V} = 0$ and $S =$ constant, the pressure and density perturbations are related by the usual expression

$$p' = C^2\rho'. \tag{65}$$

A.8 Time harmonic

When the perturbations are time-harmonic, given by (note the $+\mathrm{i}\omega t$ convention)

$$\boldsymbol{v}' = \mathrm{Re}(\boldsymbol{v}\,\mathrm{e}^{\mathrm{i}\omega t}),\ \ p' = \mathrm{Re}(p\,\mathrm{e}^{\mathrm{i}\omega t}),\ \ \rho' = \mathrm{Re}(\rho\,\mathrm{e}^{\mathrm{i}\omega t}),\ \ s' = \mathrm{Re}(s\,\mathrm{e}^{\mathrm{i}\omega t}), \tag{66}$$

(where we ignore the prime from here on), we then find in the usual complex notation

$$\mathrm{i}\omega\rho + \nabla\cdot\big(\boldsymbol{V}\rho + \boldsymbol{v}D\big) = 0, \tag{67a}$$

$$D\big(\mathrm{i}\omega + \boldsymbol{V}\cdot\nabla\big)\boldsymbol{v} + D\big(\boldsymbol{v}\cdot\nabla\big)\boldsymbol{V} + \rho\big(\boldsymbol{V}\cdot\nabla\big)\boldsymbol{V} = -\nabla p, \tag{67b}$$

$$\big(\mathrm{i}\omega + \boldsymbol{V}\cdot\nabla\big)s + \boldsymbol{v}\cdot\nabla S = 0, \tag{67c}$$

$$s = \frac{C_V}{P}p - \frac{C_P}{D}\rho. \tag{67d}$$

Note that further systematic simplifications are possible if we take into account the fact that in an engine duct the axial velocity dominates, while at the same time axial variation of the mean flow variables is relatively slow due to the (necessarily!) slowly-varying geometry.

A.9 Irrotational isentropic flow

When the flow is irrotational and isentropic everywhere (homentropic), for example in the inlet, or when we assume this condition for reasons of computational efficiency, for example in the by-pass duct, we can introduce a potential ϕ for the velocity, where $\boldsymbol{v} = \nabla\phi$ and express p as a function of ρ only. We can then integrate the momentum equation and obtain the important simplification

$$\frac{\partial}{\partial t}\phi + \tfrac{1}{2}\left|\nabla\phi\right|^2 + \frac{c^2}{\gamma - 1} = \text{constant}, \quad \frac{p}{\rho^\gamma} = \text{constant}, \tag{68}$$

which produces for the mean flow and harmonic perturbation (introduce $\phi = \Phi + \phi' = \Phi + \phi\,\mathrm{e}^{\mathrm{i}\omega t}$) the following equations

$$\nabla\cdot\big(D\nabla\Phi\big) = 0, \quad \tfrac{1}{2}\left|\nabla\Phi\right|^2 + \frac{C^2}{\gamma - 1} = \text{constant}, \quad \frac{P}{D^\gamma} = \text{constant} \tag{69a}$$

$$\mathrm{i}\omega\rho + \nabla\cdot\big(\rho\nabla\Phi + D\nabla\phi\big) = 0, \quad D\big(\mathrm{i}\omega\phi + \nabla\Phi\cdot\nabla\phi\big) + p = 0, \quad p = C^2\rho \tag{69b}$$

where the entropy equation has become a superfluous identity.

These last equations can be further simplified (by eliminating p and ρ and using the fact that $\nabla\cdot(D\nabla\Phi) = 0$) to obtain the rather general convected wave equation

$$D^{-1}\nabla\cdot\big(D\nabla\phi\big) - \big(\mathrm{i}\omega + \nabla\Phi\cdot\nabla\big)\Big[C^{-2}\big(\mathrm{i}\omega + \nabla\Phi\cdot\nabla\big)\phi\Big] = 0. \tag{70}$$

A.10 Circular symmetric geometry

To make further progress, we assume a geometry that in the immediate neighbourhood of the interface is equal to a hollow or annular cylinder with solid walls, while the mean flow is taken to be circular symmetric and axially constant.

At the solid walls where $r = R_1$ and $r = R_2$, the radial component of the velocity vanishes

$$v(x, r, \theta) = 0 \ \text{ at } \ r = R_1, \ r = R_2. \tag{71}$$

The mean flow cannot have a non-zero radial component and is a function of the radial coordinate r only. With an axial component U (in the x-direction) and a circumferential component W (in the θ-direction), the mean flow variables become

$$\boldsymbol{V} = U(r)\boldsymbol{e}_x + W(r)\boldsymbol{e}_\theta, \quad D = D(r), \quad P = P(r), \qquad S = S(r), \tag{72}$$

and the pressure is independent of x (in other words the pressure gradient vanishes) because the flow is parallel and frictionless.

All mean flow equations are now identically satisfied, except for

$$\frac{D}{r}W^2 = \frac{\partial P}{\partial r}, \tag{73}$$

and so any mean flow profiles U, W, D, P, S may be taken, so long as they satisfy the two consistency relations

$$P = \int^r \frac{D}{r}W^2\,\mathrm{d}r', \quad S = C_V\log P - C_P\log D. \tag{74}$$

Without swirl (*i.e.* $W = 0$), P is a constant, while D may vary in r if S does. A homentropic flow without swirl implies that D is a constant.

If the flow is irrotational and we want to describe it by means of a velocity potential, the most general form of the mean flow potential Φ is

$$\Phi = Ux + \Gamma\theta, \quad \text{with } \boldsymbol{V} = U\boldsymbol{e}_x + \frac{\Gamma}{r}\boldsymbol{e}_\theta \tag{75}$$

where U and Γ are constants. If the flow is also homentropic ($S = S_0 = \text{constant}$), the general forms of the pressure and density are

$$P = \Big(P_0 - \frac{\gamma - 1}{2\gamma}\, \mathrm{e}^{-S_0/C_P}\, \frac{\Gamma^2}{r^2}\Big)^{\frac{\gamma}{\gamma-1}}, \qquad D = P^{1/\gamma}\, \mathrm{e}^{-S_0/C_P}, \tag{76}$$

where P_0 is a constant.

An important special case is that of uniform flow with $\Gamma = 0$ and P and D constant.

A.11 Types of swirl

Typically, the following cases occur in a turbomachine duct

- In the inlet, the mean flow is nearly uniform and irrotational, and typically we have a thin boundary layer and a circumferential velocity or swirl given by

$$W \simeq 0 \tag{77a}$$

- In the compressor stages, the pressure increases quickly and the boundary layer is most probably thin.

- In the compressor, behind a stator or guide vanes and before a rotor, the mean flow is close to that of a rigid body rotation and the circumferential velocity is typically

$$W \simeq \Omega r \tag{77b}$$

- In the compressor, behind a rotor and before a stator or guide vanes, the mean flow also contains swirl, for example in the form of a free axial vortex. The circumferential velocity is then typically

$$W \simeq \Omega r + \frac{\Gamma}{r} \tag{77c}$$

- Behind the compressor, for example in the bypass duct, the swirl W should again be small, but the boundary layer may be significant acoustically (refraction).

We will not examine here any other mean flow profiles. It should, however, be noted that we will assume a discrete spectrum for the modal expansion to be introduced below (*normal modes approach*). Although the matter is not completely settled yet, there is strong evidence in the literature that a discrete set of modes is not a complete basis of the solution space of the present equations considered if the mean flow is arbitrary. At least in principle, care should be taken when the profile allows critical layers (the radial position where the convected derivative $(\mathrm{i}\omega + \boldsymbol{V}\cdot\nabla)$ vanishes). Only if the mean flow is simple enough (as in the above cases) does the modal spectrum appear to be discrete everywhere.

B Acoustic equations with circular symmetric geometry

The acoustic equations, corresponding to the circular symmetric mean flow introduced in section A.10, are as follows. For the perturbation velocity vector

$$\boldsymbol{v} = u\boldsymbol{e}_x + v\boldsymbol{e}_r + w\boldsymbol{e}_\theta, \tag{78}$$

the harmonic perturbation equations are written out in full (a prime denotes a derivative with respect to r of the mean flow variable) in the subsections below*.

B.1 With swirl and variable entropy

$$\Big(\mathrm{i}\omega + U\frac{\partial}{\partial x} + \frac{W}{r}\frac{\partial}{\partial\theta}\Big)\rho + D\Big(\frac{\partial u}{\partial x} + \frac{1}{r}\frac{\partial}{\partial r}(rv) + \frac{1}{r}\frac{\partial w}{\partial\theta}\Big) + D'v = 0 \tag{79a}$$

$$D\Big(\mathrm{i}\omega + U\frac{\partial}{\partial x} + \frac{W}{r}\frac{\partial}{\partial\theta}\Big)u + DU'v + \frac{\partial p}{\partial x} = 0 \tag{79b}$$

$$D\Big(\mathrm{i}\omega + U\frac{\partial}{\partial x} + \frac{W}{r}\frac{\partial}{\partial\theta}\Big)v - \frac{2DW}{r}w - \frac{W^2}{r}\rho + \frac{\partial p}{\partial r} = 0 \tag{79c}$$

$$D\Big(\mathrm{i}\omega + U\frac{\partial}{\partial x} + \frac{W}{r}\frac{\partial}{\partial\theta}\Big)w + \frac{DW}{r}v + DW'v + \frac{1}{r}\frac{\partial p}{\partial\theta} = 0 \tag{79d}$$

$$\Big(\mathrm{i}\omega + U\frac{\partial}{\partial x} + \frac{W}{r}\frac{\partial}{\partial\theta}\Big)s + S'v = 0 \tag{79e}$$

By using relation (67d) between s, p and ρ and equation (79a), s can be eliminated and equation (79e) replaced by

$$\Big(\mathrm{i}\omega + U\frac{\partial}{\partial x} + \frac{W}{r}\frac{\partial}{\partial\theta}\Big)\big(p - C^2\rho\big) + \Big(\frac{DW^2}{r} - C^2D'\Big)v = 0 \tag{79f}$$

*Recall the following identities in cylindrical co-ordinates for vector fields $\boldsymbol{v}$ and $\boldsymbol{V}$ and a scalar ϕ

$$\begin{aligned}
\nabla\cdot\boldsymbol{v} &= \tfrac{\partial}{\partial x}u + \tfrac{\partial}{\partial r}v + \tfrac{1}{r}v + \tfrac{1}{r}\tfrac{\partial}{\partial\theta}w\\
\boldsymbol{V}\cdot\nabla\boldsymbol{v} &= \big(U\tfrac{\partial}{\partial x}u + V\tfrac{\partial}{\partial r}u + \frac{1}{r}W\tfrac{\partial}{\partial\theta}u\big)\boldsymbol{e}_x + \big(U\tfrac{\partial}{\partial x}v + V\tfrac{\partial}{\partial r}v + \tfrac{1}{r}W\big(\tfrac{\partial}{\partial\theta}v - w\big)\big)\boldsymbol{e}_r\\
&\qquad + \big(U\tfrac{\partial}{\partial x}w + V\tfrac{\partial}{\partial r}w + \tfrac{1}{r}W(\tfrac{\partial}{\partial\theta}w + v)\big)\boldsymbol{e}_\theta\\
\nabla\times\boldsymbol{v} &= \big(\tfrac{\partial}{\partial r}w + \tfrac{1}{r}w - \tfrac{1}{r}\tfrac{\partial}{\partial\theta}v\big)\boldsymbol{e}_x + \big(\tfrac{1}{r}\tfrac{\partial}{\partial\theta}u - \tfrac{\partial}{\partial x}w\big)\boldsymbol{e}_r + \big(\tfrac{\partial}{\partial x}v - \tfrac{\partial}{\partial r}u\big)\boldsymbol{e}_\theta\\
\nabla\phi &= \tfrac{\partial}{\partial r}\phi\boldsymbol{e}_r + \tfrac{1}{r}\tfrac{\partial}{\partial\theta}\phi\boldsymbol{e}_\theta + \tfrac{\partial}{\partial x}\phi\boldsymbol{e}_x.
\end{aligned}$$

B.2 Without swirl and variable entropy

Without swirl the harmonic perturbation equations are

$$\Big(\mathrm{i}\omega + U\frac{\partial}{\partial x}\Big)\rho + D\Big(\frac{\partial u}{\partial x} + \frac{1}{r}\frac{\partial}{\partial r}(rv) + \frac{1}{r}\frac{\partial w}{\partial \theta}\Big) + D'v = 0 \tag{80a}$$

$$D\Big(\mathrm{i}\omega + U\frac{\partial}{\partial x}\Big)u + DU'v + \frac{\partial p}{\partial x} = 0 \tag{80b}$$

$$D\Big(\mathrm{i}\omega + U\frac{\partial}{\partial x}\Big)v + \frac{\partial p}{\partial r} = 0 \tag{80c}$$

$$D\Big(\mathrm{i}\omega + U\frac{\partial}{\partial x}\Big)w + \frac{1}{r}\frac{\partial p}{\partial \theta} = 0 \tag{80d}$$

$$\Big(\mathrm{i}\omega + U\frac{\partial}{\partial x}\Big)(p - C^2\rho) - C^2 D'v = 0 \tag{80e}$$

B.3 Homentropic without swirl

Without swirl and entropy variations the harmonic perturbation equations are

$$\Big(\mathrm{i}\omega + U\frac{\partial}{\partial x}\Big)\rho + D\Big(\frac{\partial u}{\partial x} + \frac{1}{r}\frac{\partial}{\partial r}(rv) + \frac{1}{r}\frac{\partial w}{\partial \theta}\Big) = 0 \tag{81a}$$

$$D\Big(\mathrm{i}\omega + U\frac{\partial}{\partial x}\Big)u + DU'v + \frac{\partial p}{\partial x} = 0 \tag{81b}$$

$$D\Big(\mathrm{i}\omega + U\frac{\partial}{\partial x}\Big)v + \frac{\partial p}{\partial r} = 0 \tag{81c}$$

$$D\Big(\mathrm{i}\omega + U\frac{\partial}{\partial x}\Big)w + \frac{1}{r}\frac{\partial p}{\partial \theta} = 0 \tag{81d}$$

$$p - C^2\rho = 0 \tag{81e}$$

B.4 Irrotational homentropic flow

When the flow is irrotational and homentropic, we can introduce a potential in the form of equation (75) and integrate the momentum equation to get (69). P and D are in the form of equation (76), while U and Γ are constants. The result is the expressions:

$$\Big(\mathrm{i}\omega + U\frac{\partial}{\partial x} + \frac{\Gamma}{r^2}\frac{\partial}{\partial \theta}\Big)\rho + D\Big(\frac{\partial^2\phi}{\partial x^2} + \frac{1}{r}\frac{\partial}{\partial r}\Big(r\frac{\partial\phi}{\partial r}\Big) + \frac{1}{r^2}\frac{\partial^2\phi}{\partial\theta^2}\Big) + D'\frac{\partial\phi}{\partial r} = 0 \tag{82a}$$

$$D\Big(\mathrm{i}\omega + U\frac{\partial}{\partial x} + \frac{\Gamma}{r^2}\frac{\partial}{\partial\theta}\Big)\phi + p = 0 \tag{82b}$$

$$p - C^2\rho = 0 \tag{82c}$$

B.5 Uniform mean flow

The simplest, but therefore the most important configuration, is the one with uniform mean flow. Note that this does **not** exactly imply irrotational and isentropic perturbations.

Axial mean velocity U, mean pressure P, density D and sound speed C are constants, so we have

$$\Big(\mathrm{i}\omega + U\frac{\partial}{\partial x}\Big)\rho + D\Big(\frac{\partial u}{\partial x} + \frac{1}{r}\frac{\partial}{\partial r}(rv) + \frac{1}{r}\frac{\partial w}{\partial \theta}\Big) = 0, \tag{83a}$$

$$D\Big(\mathrm{i}\omega + U\frac{\partial}{\partial x}\Big)u + \frac{\partial p}{\partial x} = 0, \tag{83b}$$

$$D\Big(\mathrm{i}\omega + U\frac{\partial}{\partial x}\Big)v + \frac{\partial p}{\partial r} = 0, \tag{83c}$$

$$D\Big(\mathrm{i}\omega + U\frac{\partial}{\partial x}\Big)w + \frac{1}{r}\frac{\partial p}{\partial \theta} = 0, \tag{83d}$$

$$\Big(\mathrm{i}\omega + U\frac{\partial}{\partial x}\Big)\big(p - C^2\rho\big) = 0. \tag{83e}$$

We then split the perturbation velocity into a vortical part and an irrotational part by introducing the vector potential (stream function) $\boldsymbol{\Psi}$ and scalar potential ϕ as follows (see the footnote on page 54)

$$\boldsymbol{v} = \nabla\times\boldsymbol{\Psi} + \nabla\phi. \tag{84}$$

If desired, the arbitrariness in $\boldsymbol{\Psi}$ (we may add any ∇f, since $\nabla\times\nabla f \equiv 0$) may be removed by adding the gauge condition $\nabla\cdot\boldsymbol{\Psi} = 0$, such that the vorticity is given by

$$\boldsymbol{\xi} = \nabla\times\boldsymbol{v} = \nabla(\nabla\cdot\boldsymbol{\Psi}) - \nabla^2\boldsymbol{\Psi} = -\nabla^2\boldsymbol{\Psi}. \tag{85}$$

Since the divergence of a curl is zero, $\nabla\cdot\boldsymbol{v} = \nabla\cdot(\nabla\times\boldsymbol{\Psi} + \nabla\phi) = \nabla^2\phi$ and equation (83a) becomes

$$\Big(\mathrm{i}\omega + U\frac{\partial}{\partial x}\Big)\rho + D\nabla^2\phi = 0 \tag{86}$$

From the equations (83b-d), given in vector form by

$$D\Big(\mathrm{i}\omega + U\frac{\partial}{\partial x}\Big)\big(\nabla\times\boldsymbol{\Psi} + \nabla\phi\big) + \nabla p = 0, \tag{87}$$

we readily see that by taking the divergence of equation (87) and using equations (83e) and (86), we can eliminate ϕ and ρ to obtain the convected reduced wave equation for the pressure

$$C^2\nabla^2 p - \Big(\mathrm{i}\omega + U\frac{\partial}{\partial x}\Big)^2 p = 0. \tag{88}$$

(Note that we did not assume the isentropy relation $p = C^2\rho$.) With some care, especially taking due notice of the singular edge behaviour, this equation may be transformed to the ordinary reduced wave equation by allowing

$$p(x, r, \theta; \omega) = \widetilde{p}(X, r, \theta; \Omega)\exp(\mathrm{i}\tfrac{\Omega M}{C}X), \tag{89}$$

$$\text{where}\quad x = \beta X,\ \omega = \beta\Omega,\ M = \frac{U}{C},\ \beta = \sqrt{1 - M^2}.$$

In addition, by taking the curl of equations 83(b-d) we can eliminate p and ϕ to produce an equation for the vorticity:

$$-\Big(\mathrm{i}\omega + U\frac{\partial}{\partial x}\Big)\nabla^2\boldsymbol{\Psi} = \Big(\mathrm{i}\omega + U\frac{\partial}{\partial x}\Big)\boldsymbol{\xi} = 0. \tag{90}$$

Summarizing, we have found a convected wave equation (88) for the pressure, and equations that describe simple mean flow convection for the entropy (83e) and for the vorticity (90). These three equations are (in the uniform mean flow case) completely independent and therefore describe independent quantities. Since the velocity fluctuations are determined by the sum of acoustic contributions (connected to p) and vortical contributions (connected to $\boldsymbol{\xi}$), acoustic information cannot be obtained from the velocity field alone if the flow is **not irrotational** (as in the bypass duct, or anywhere behind a rotor or a stator). In such a situation, information on the acoustic properties of the flow *can only* be yielded directly from the pressure distribution p. Thus, the direction of the acoustic waves may have to be determined by examining axial changes in pressure using either its axial derivative $\frac{\partial}{\partial x}p$ or by comparing pressure values at neighbouring interfaces. This important point must be taken into account in any development of a robust and reliable matching strategy.

C Circumferential Fourier decomposition

In view of the circumferential periodicity of the solution, the dependent variables can be written as a Fourier series in θ. Because of the linearity and θ-independence of the equations, the problem can then be solved per Fourier mode. Here we have

$$\boldsymbol{v} = \sum_{m=-\infty}^{\infty} \boldsymbol{v}_m(x,r)\,\mathrm{e}^{-\mathrm{i}m\theta}, \quad p = \sum_{m=-\infty}^{\infty} p_m(x,r)\,\mathrm{e}^{-\mathrm{i}m\theta}, \quad \rho = \sum_{m=-\infty}^{\infty} \rho_m(x,r)\,\mathrm{e}^{-\mathrm{i}m\theta}\,. \tag{91}$$

The equations for each case reduce to:

C.1 With swirl and variable entropy

$$\Big(\mathrm{i}\omega + U\frac{\partial}{\partial x} - \frac{\mathrm{i}mW}{r}\Big)\rho_m + D\Big(\frac{\partial u_m}{\partial x} + \frac{1}{r}\frac{\partial}{\partial r}(r v_m) - \frac{\mathrm{i}m}{r}w_m\Big) + D' v_m = 0 \tag{92a}$$

$$D\Big(\mathrm{i}\omega + U\frac{\partial}{\partial x} - \frac{\mathrm{i}mW}{r}\Big)u_m + DU' v_m + \frac{\partial p_m}{\partial x} = 0 \tag{92b}$$

$$D\Big(\mathrm{i}\omega + U\frac{\partial}{\partial x} - \frac{\mathrm{i}mW}{r}\Big)v_m - \frac{2DW}{r}w_m - \frac{W^2}{r}\rho_m + \frac{\partial p_m}{\partial r} = 0 \tag{92c}$$

$$D\Big(\mathrm{i}\omega + U\frac{\partial}{\partial x} - \frac{\mathrm{i}mW}{r}\Big)w_m + \frac{DW}{r}v_m + DW' v_m - \frac{\mathrm{i}m}{r}p_m = 0 \tag{92d}$$

$$\Big(\mathrm{i}\omega + U\frac{\partial}{\partial x} - \frac{\mathrm{i}mW}{r}\Big)(p_m - C^2\rho_m) + \Big(\frac{DW^2}{r} - C^2 D'\Big)v_m = 0 \tag{92e}$$

C.2 Without swirl and variable entropy

$$\Big(\mathrm{i}\omega + U\frac{\partial}{\partial x}\Big)\rho_m + D\Big(\frac{\partial u_m}{\partial x} + \frac{1}{r}\frac{\partial}{\partial r}(r v_m) - \frac{\mathrm{i}m}{r}w_m\Big) + D' v_m = 0 \tag{93a}$$

$$D\Big(\mathrm{i}\omega + U\frac{\partial}{\partial x}\Big)u_m + DU' v_m + \frac{\partial p_m}{\partial x} = 0 \tag{93b}$$

$$D\Big(\mathrm{i}\omega + U\frac{\partial}{\partial x}\Big)v_m + \frac{\partial p_m}{\partial r} = 0 \tag{93c}$$

$$D\Big(\mathrm{i}\omega + U\frac{\partial}{\partial x}\Big)w_m - \frac{\mathrm{i}m}{r}p_m = 0 \tag{93d}$$

$$\Big(\mathrm{i}\omega + U\frac{\partial}{\partial x}\Big)(p_m - C^2\rho_m) - C^2 D' v_m = 0 \tag{93e}$$

C.3 Homentropic without swirl

$$\Big(\mathrm{i}\omega + U\frac{\partial}{\partial x}\Big)\rho_m + D\Big(\frac{\partial u_m}{\partial x} + \frac{1}{r}\frac{\partial}{\partial r}(r v_m) - \frac{\mathrm{i}m}{r}w_m\Big) = 0 \tag{94a}$$

$$D\Big(\mathrm{i}\omega + U\frac{\partial}{\partial x}\Big)u_m + DU' v_m + \frac{\partial p_m}{\partial x} = 0 \tag{94b}$$

$$D\Big(\mathrm{i}\omega + U\frac{\partial}{\partial x}\Big)v_m + \frac{\partial p_m}{\partial r} = 0 \tag{94c}$$

$$D\Big(\mathrm{i}\omega + U\frac{\partial}{\partial x}\Big)w_m - \frac{\mathrm{i}m}{r}p_m = 0 \tag{94d}$$

$$p_m - C^2\rho_m = 0 \tag{94e}$$

C.4 Irrotational homentropic flow

$$\Big(\mathrm{i}\omega + U\frac{\partial}{\partial x} - \frac{\mathrm{i}m\Gamma}{r^2}\Big)\rho + D\Big(\frac{\partial^2\phi}{\partial x^2} + \frac{1}{r}\frac{\partial}{\partial r}\big(r\frac{\partial\phi}{\partial r}\big) - \frac{m^2}{r^2}\phi\Big) + D'\frac{\partial\phi}{\partial r} = 0 \tag{95a}$$

$$D\Big(\mathrm{i}\omega + U\frac{\partial}{\partial x} - \frac{\mathrm{i}m\Gamma}{r^2}\Big)\phi + p = 0 \tag{95b}$$

$$p - C^2\rho = 0 \tag{95c}$$

C.5 Uniform mean flow with irrotational isentropic perturbations

$$\Big(\mathrm{i}\omega + U\frac{\partial}{\partial x}\Big)\rho + D\Big(\frac{\partial^2\phi}{\partial x^2} + \frac{1}{r}\frac{\partial}{\partial r}\big(r\frac{\partial\phi}{\partial r}\big) - \frac{m^2}{r^2}\phi\Big) = 0 \tag{96a}$$

$$D\Big(\mathrm{i}\omega + U\frac{\partial}{\partial x}\Big)\phi + p = 0 \tag{96b}$$

$$p - C^2\rho = 0 \tag{96c}$$

D Normal modes

In order to solve our present matching problem, we need to be able to distinguish incoming and outgoing (left- and right-running) waves. We do this by solving the above equations, assuming that they represent the field locally near the interface.

A general way to solve the equations (in a locally parallel duct section), which are still partial differential equations in r and x, involves a Fourier transformation in x of the form

$$f(x,r) = \int_{-\infty}^{\infty} \hat{f}(r;\kappa)\, \mathrm{e}^{-\mathrm{i}\kappa x}\, \mathrm{d}\kappa \tag{97}$$

The resulting equations to be solved then become just ordinary differential equations in r. It will appear that the Fourier transformed solution has an infinite number of poles in the complex axial wave number plane, corresponding to the duct modes. If the Fourier transformed solution is meromorphic (analytic except for isolated poles $\kappa = \kappa_\mu$), the inverse transform can be evaluated and the solution in x-space can be written as an infinite modal sum. This appears to be the case if the mean flow is sufficiently simple (uniform, etc.). Symbolically, this is represented as

$$f(x,r) = \sum_{\mu=1}^{\infty} F_\mu^+(r)\, \mathrm{e}^{-\mathrm{i}\kappa_\mu^+ x} + \sum_{\mu=1}^{\infty} F_\mu^-(r)\, \mathrm{e}^{-\mathrm{i}\kappa_\mu^- x} \tag{98}$$

where the modal wave numbers κ_μ^+ and κ_μ^- correspond to right- and left-running modes respectively.

In general cases, the Fourier-transformed solution is not meromorphic and the solution has to be described by a modal sum plus an integral over the continuous part of the wave number spectrum. For example,

$$f(x,r) = \sum_{\mu=1}^{\infty} F_\mu^+(r)\, \mathrm{e}^{-\mathrm{i}\kappa_\mu^+ x} + \sum_{\mu=1}^{\infty} F_\mu^-(r)\, \mathrm{e}^{-\mathrm{i}\kappa_\mu^- x} + \int_{\mathcal{C}} \hat{f}(r;\kappa)\, \mathrm{e}^{-\mathrm{i}\kappa x}\, \mathrm{d}\kappa \tag{99}$$

Usually, this supplementary part seems to be of minor importance acoustically, as it refers to mainly hydrodynamic-type perturbations. Furthermore, it is also computationally very inconvenient. Therefore, we will ignore it here altogether and just assume solutions of the form

$$\boldsymbol{v}_m = \sum_{\mu=-\infty}^{\infty} \boldsymbol{v}_{m\mu}(r)\, \mathrm{e}^{-\mathrm{i}\kappa_{m\mu} x}, \quad p_m = \sum_{\mu=-\infty}^{\infty} p_{m\mu}(r)\, \mathrm{e}^{-\mathrm{i}\kappa_{m\mu} x}, \quad s_m = \sum_{\mu=-\infty}^{\infty} s_{m\mu}(r)\, \mathrm{e}^{-\mathrm{i}\kappa_{m\mu} x} \tag{100}$$

(the distinction between left and right running will be made later) leading to the following reduced sets of equations. We introduce the following scaled variables for convenience

$$\Omega_{m\mu} = \omega - \kappa_{m\mu} U, \quad \Omega_{m\mu}^{(W)} = \omega - \kappa_{m\mu} U - \frac{mW}{r}, \quad \Omega_{m\mu}^{(\Gamma)} = \omega - \kappa_{m\mu} U - \frac{m\Gamma}{r^2}. \tag{101}$$

D.1 With swirl and variable entropy

$$\mathrm{i}\Omega^{(W)}_{m\mu}\rho_{m\mu} + D\Big(-\mathrm{i}\kappa_{m\mu}u_{m\mu} + \frac{1}{r}\frac{\partial}{\partial r}(r\,v_{m\mu}) - \frac{\mathrm{i}m}{r}w_{m\mu}\Big) + D'v_{m\mu} = 0 \tag{102a}$$

$$\mathrm{i}D\Omega^{(W)}_{m\mu}u_{m\mu} + DU'v_{m\mu} - \mathrm{i}\kappa_{m\mu}p_{m\mu} = 0 \tag{102b}$$

$$\mathrm{i}D\Omega^{(W)}_{m\mu}v_{m\mu} - \frac{2DW}{r}w_{m\mu} - \frac{W^2}{r}\rho_{m\mu} + \frac{\partial p_{m\mu}}{\partial r} = 0 \tag{102c}$$

$$\mathrm{i}D\Omega^{(W)}_{m\mu}w_{m\mu} + \frac{DW}{r}v_{m\mu} + DW'v_{m\mu} - \frac{\mathrm{i}m}{r}p_{m\mu} = 0 \tag{102d}$$

$$\mathrm{i}\Omega^{(W)}_{m\mu}\big(p_{m\mu} - C^2\rho_{m\mu}\big) + \Big(\frac{DW^2}{r} - C^2D'\Big)v_{m\mu} = 0 \tag{102e}$$

D.2 Without swirl and variable entropy

$$\mathrm{i}\Omega_{m\mu}\rho_{m\mu} + D\Big(-\mathrm{i}\kappa_{m\mu}u_{m\mu} + \frac{1}{r}\frac{\partial}{\partial r}(r\,v_{m\mu}) - \frac{\mathrm{i}m}{r}w_{m\mu}\Big) + D'v_{m\mu} = 0 \tag{103a}$$

$$\mathrm{i}D\Omega_{m\mu}u_{m\mu} + DU'v_{m\mu} - \mathrm{i}\kappa_{m\mu}p_{m\mu} = 0 \tag{103b}$$

$$\mathrm{i}D\Omega_{m\mu}v_{m\mu} + \frac{\partial p_{m\mu}}{\partial r} = 0 \tag{103c}$$

$$\mathrm{i}D\Omega_{m\mu}w_{m\mu} - \frac{\mathrm{i}m}{r}p_{m\mu} = 0 \tag{103d}$$

$$\mathrm{i}\Omega_{m\mu}\big(p_{m\mu} - C^2\rho_{m\mu}\big) - C^2D'v_{m\mu} = 0 \tag{103e}$$

which becomes, after eliminating all variables but $p_{m\mu}$, the equation

$$\frac{\Omega_{m\mu}D}{r}\frac{\partial}{\partial r}\Big(\frac{r}{\Omega_{m\mu}D}\frac{\partial}{\partial r}p_{m\mu}\Big) + \frac{\kappa_{m\mu}U'}{\Omega_{m\mu}}\frac{\partial}{\partial r}p_{m\mu} + \Big(\frac{\Omega^2_{m\mu}}{C^2} - \kappa^2_{m\mu} - \frac{m^2}{r^2}\Big)p_{m\mu} = 0. \tag{103f}$$

D.3 Homentropic without swirl

$$\mathrm{i}\Omega_{m\mu}\rho_{m\mu} + D\Big(-\mathrm{i}\kappa_{m\mu}u_{m\mu} + \frac{1}{r}\frac{\partial}{\partial r}(r\,v_{m\mu}) - \frac{\mathrm{i}m}{r}w_{m\mu}\Big) = 0 \tag{104a}$$

$$\mathrm{i}D\Omega_{m\mu}u_{m\mu} + DU'v_{m\mu} - \mathrm{i}\kappa_{m\mu}p_{m\mu} = 0 \tag{104b}$$

$$\mathrm{i}D\Omega_{m\mu}v_{m\mu} + \frac{\partial p_{m\mu}}{\partial r} = 0 \tag{104c}$$

$$\mathrm{i}D\Omega_{m\mu}w_{m\mu} - \frac{\mathrm{i}m}{r}p_{m\mu} = 0 \tag{104d}$$

$$p_{m\mu} - C^2\rho_{m\mu} = 0. \tag{104e}$$

This becomes for $p_{m\mu}$ (because D is a constant)

$$\frac{\Omega_{m\mu}}{r}\frac{\partial}{\partial r}\Big(\frac{r}{\Omega_{m\mu}}\frac{\partial}{\partial r}p_{m\mu}\Big) + \frac{\kappa_{m\mu}U'}{\Omega_{m\mu}}\frac{\partial}{\partial r}p_{m\mu} + \Big(\frac{\Omega^2_{m\mu}}{C^2} - \kappa^2_{m\mu} - \frac{m^2}{r^2}\Big)p_{m\mu} = 0. \tag{104f}$$

D.4 Irrotational homentropic flow

$$\mathrm{i}\Omega^{(\Gamma)}_{m\mu}\rho_{m\mu} + D\Big(-\kappa^2_{m\mu}\phi_{m\mu} + \frac{1}{r}\frac{\partial}{\partial r}\big(r\frac{\partial\phi_{m\mu}}{\partial r}\big) - \frac{m^2}{r^2}\phi_{m\mu}\Big) + D'\frac{\partial\phi_{m\mu}}{\partial r} = 0 \tag{105a}$$

$$\mathrm{i}D\Omega^{(\Gamma)}_{m\mu}\phi_{m\mu} + p_{m\mu} = 0 \tag{105b}$$

$$p_{m\mu} - C^2\rho_{m\mu} = 0 \tag{105c}$$

This becomes for $\phi_{m\mu}$

$$\frac{1}{rD}\frac{\partial}{\partial r}\big(rD\frac{\partial\phi_{m\mu}}{\partial r}\big) + \Big(\Big\{\frac{\Omega^{(\Gamma)}_{m\mu}}{C}\Big\}^2 - \kappa^2_{m\mu} - \frac{m^2}{r^2}\Big)\phi_{m\mu} = 0 \tag{105d}$$

D.5 Uniform mean flow with irrotational isentropic perturbations

$$\mathrm{i}\Omega_{m\mu}\rho_{m\mu} + D\Big(-\kappa^2_{m\mu}\phi_{m\mu} + \frac{1}{r}\frac{\partial}{\partial r}\big(r\frac{\partial\phi_{m\mu}}{\partial r}\big) - \frac{m^2}{r^2}\phi_{m\mu}\Big) = 0 \tag{106a}$$

$$\mathrm{i}D\Omega_{m\mu}\phi_{m\mu} + p_{m\mu} = 0 \tag{106b}$$

$$p_{m\mu} - C^2\rho_{m\mu} = 0 \tag{106c}$$

This becomes, finally, for $\phi_{m\mu}$

$$\frac{1}{r}\frac{\partial}{\partial r}\big(r\frac{\partial\phi_{m\mu}}{\partial r}\big) + \Big(\frac{\Omega^2_{m\mu}}{C^2} - \kappa^2_{m\mu} - \frac{m^2}{r^2}\Big)\phi_{m\mu} = 0 \tag{106d}$$

D.6 The modes

The resulting differential equations and boundary conditions are to be solved as eigenvalue problems, with, in general, complex eigenvalues $\kappa_{m\mu}$. This can be done in various ways that will not be discussed further here. For example, the uniform flow case allows an analytical solution and therefore is a particularly interesting case, but for the other more general cases numerical methods are necessary to obtain solutions.

In the present application it is very important to distinguish the incoming and outgoing (left- and right-running) waves. The set of poles corresponding to modes decaying in the positive x-direction are found (in this notation convention!) in the lower complex half plane $\mathrm{Im}(\kappa) < 0$. Apart from any instabilities[*], these modes are entirely right-running. Further, the set of poles corresponding to modes decaying in the negative x-direction are found in the upper complex half plane $\mathrm{Im}(\kappa) > 0$ and, apart from any instabilities, these modes are entirely left-running. The poles found along the real κ-axis are not immediately recognized as either right or left running. Without mean flow, the direction of the wave corresponds with the modal phase velocity κ_μ/ω. With flow this is not exactly the case anymore and some extra care must be taken. One possible way to classify the modes is by taking the hard-wall limit of a duct with soft (dissipative) walls.

[*]Note that a necessary and sufficient condition for stability of a rotating incompressible inviscid fluid is $\frac{\mathrm{d}}{\mathrm{d}r}(Wr)^2 > 0$, (Rayleigh, see [22]).

Bibliography

[1] B.A. SINGER, K.S. BRENTNER, D.P. LOCKARD AND G.M. LILLEY, Simulation of acoustic scattering from a trailing edge, *AIAA-99-0231*, 1999.

[2] D.P. LOCKARD, An overview of computational aeroacoustic modeling at NASA Langley, *10th Thermal and Fluids Analysis Workshop, Huntsville, Alabama, Sept 13-17*, 1999.

[3] R.P. DOUGHERTY, A wave splitting technique for nacelle acoustic propagation, *AIAA-97-1652*, 1997.

[4] R.P. DOUGHERTY, A parabolic approximation for flow effects on sound propagation in nonuniform softwall ducts, *AIAA-99-1822*, 1999.

[5] V.V. GOLUBEV AND H.M. ATASSI, Sound propagation in an annular duct with mean potential swirling flow, *J. Sound Vib.*, **198** (5), p. 601–616, 1996.

[6] V.V. GOLUBEV AND H.M. ATASSI, Acoustic-vorticity waves in swirling flows, *J. Sound Vib.*, **209** (2), p. 203–222, 1998.

[7] R.J. NIJBOER, Eigenvalues and eigenfunctions of ducted swirling flows, *AIAA Paper 2001-2178, 7th AIAA/CEAS Aeroacoustics Conference, 28-30 May 2001, Maastricht, The Netherlands. (NLR-TP-2001-141)*, 2001.

[8] R.J. NIJBOER, Sound propagation in ducted swirling flows, *NLR-TR-2001-340*, TurboNoiseCFD Deliverable D2.6, 2001.

[9] A.J. COOPER AND N. PEAKE, Propagation of unsteady disturbances in a slowly varying duct with mean swirling flow, *J. Fluid Mech.*, **445**, 207–234, 2001.

[10] R.H. CANTRELL AND R.W. HART, Interaction between sound and flow in acoustic cavities: mass, momentum and energy considerations, *J. Acoust. Soc. Am.* **36**, 697-706, 1964.

[11] C.L. MORFEY, Acoustic energy in non-uniform flows, *J. Sound Vib.*, **14**, 159-169, 1971.

[12] M.K. MYERS, An exact energy corollary for homentropic flow. *J. Sound Vib.*, **109**, 277-284, 1986.

[13] M.K. MYERS, Transport of energy by disturbances in arbitrary steady flows. *J. Fluid Mech.*, **226**, 383-400, 1991.

[14] A.G. WILSON, Application of CFD to wake/aerofoil interaction noise - a flat plate validation case. *AIAA 2001-2135*, 2001.

[15] A.H. NAYFEH AND D.P. TELIONIS, Acoustic propagation in ducts of varying cross sections, *J. Acoust. Soc. Am.*, **54**(6), 1654–1661, 1973.

[16] S.W. RIENSTRA, Sound transmission in slowly varying circular and annular ducts with flow, *J. Fluid Mech.*, **380**, 279–296, 1999.

[17] G.N. WATSON, *The theory of Bessel Functions*, 2nd edition, Cambridge University Press, 1966.

[18] M.K. MYERS, On the acoustic boundary condition in the presence of flow. *J. Sound Vib.*, **71**(3), 429-434, 1980.

[19] S.W. RIENSTRA, Cut-on, cut-off transition of sound in slowly varying flow ducts. *Aerotechnica - Missili e Spazio, special issue in memory of Prof D.G. Crighton,* **79**, nos. 3-4, 93-97. (edited by L. Morino and N. Peake), 2000.

[20] N.C. OVENDEN, Near cut-on/cut-off transition in lined ducts with flow. *AIAA 2002-2445, 8th AIAA/CEAS Aeroacoustics conference, 17-19 June 2002, Breckenridge, Colorado*, 2002.

[21] L.D. LANDAU AND E.M. LIFSHITZ, *Fluid Mechanics*, 2nd edition, Pergamon Press, Oxford, 1987.

[22] C.K.W. TAM AND L. AURIAULT, The wave modes in ducted swirling flows, *J. Fluid Mech.,* **371**, p. 1–20, (*AIAA-98-2280*), 1998.